RESEARCH ARTICLE

MYC Levels Regulate Metastatic Heterogeneity in Pancreatic Adenocarcinoma

Ravikanth Maddipati[1,2], Robert J. Norgard[3], Timour Baslan[4], Komal S. Rathi[5,6], Amy Zhang[7], Asal Saeid[1], Taku Higashihara[1], Feng Wu[1], Angad Kumar[1], Valli Annamalai[1], Saurav Bhattacharya[1], Pichai Raman[5,6], Christian A. Adkisson[8], Jason R. Pitarresi[3], Maximilian D. Wengyn[3], Taiji Yamazoe[3], Jinyang Li[3], David Balli[3], Michael J. LaRiviere[9], Tuong-Vi C. Ngo[2], Ian W. Folkert[3,10], Ian D. Millstein[3], Jonathan Bermeo[4,11], Erica L. Carpenter[12], John C. McAuliffe[8], Maja H. Oktay[13], Rolf A. Brekken[2], Scott W. Lowe[4], Christine A. Iacobuzio-Donahue[11,14], Faiyaz Notta[7,15,16], and Ben Z. Stanger[3,17]

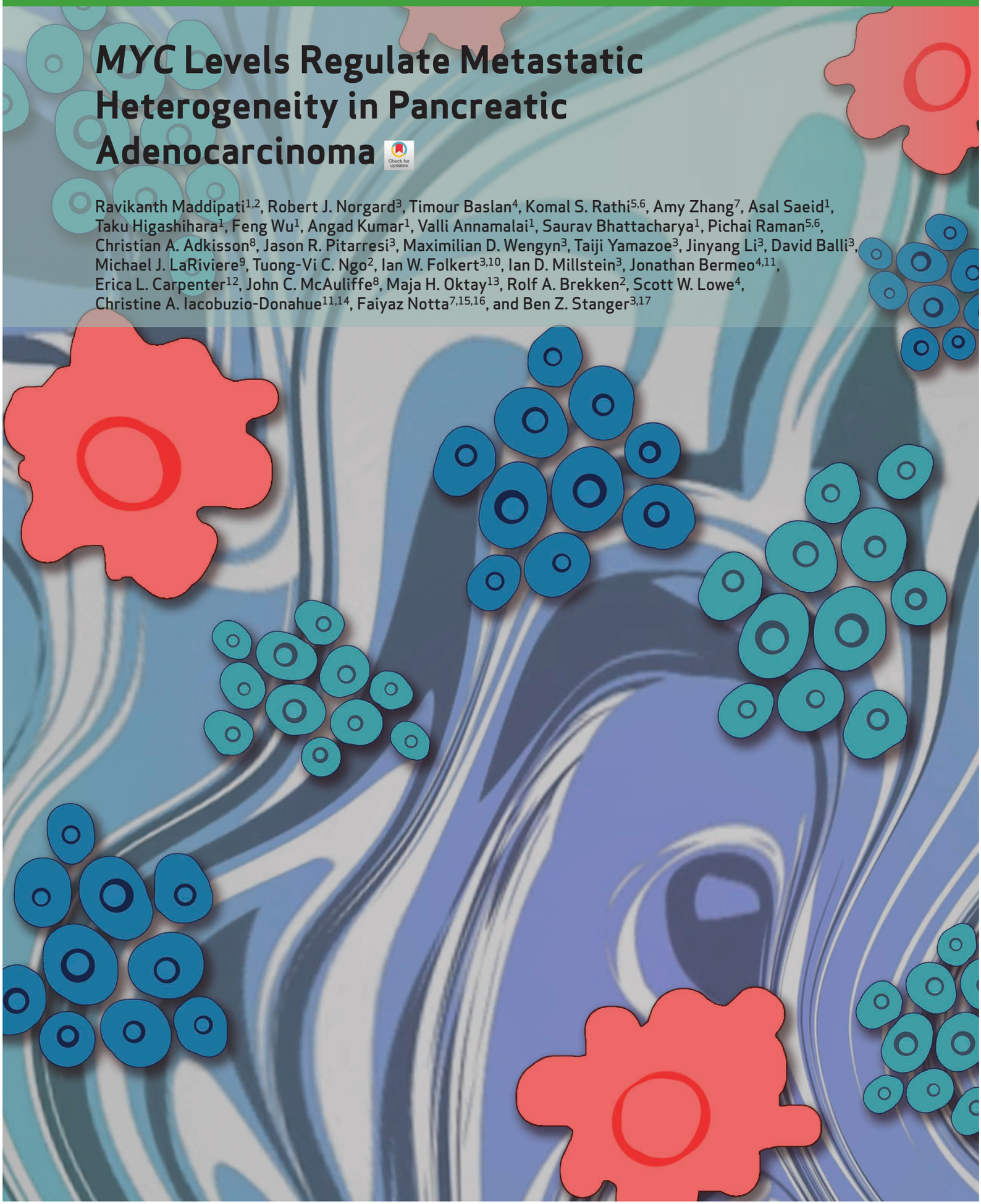

ABSTRACT The degree of metastatic disease varies widely among patients with cancer and affects clinical outcomes. However, the biological and functional differences that drive the extent of metastasis are poorly understood. We analyzed primary tumors and paired metastases using a multifluorescent lineage-labeled mouse model of pancreatic ductal adenocarcinoma (PDAC)—a tumor type in which most patients present with metastases. Genomic and transcriptomic analysis revealed an association between metastatic burden and gene amplification or transcriptional upregulation of *MYC* and its downstream targets. Functional experiments showed that MYC promotes metastasis by recruiting tumor-associated macrophages, leading to greater bloodstream intravasation. Consistent with these findings, metastatic progression in human PDAC was associated with activation of MYC signaling pathways and enrichment for *MYC* amplifications specifically in metastatic patients. Collectively, these results implicate MYC activity as a major determinant of metastatic burden in advanced PDAC.

SIGNIFICANCE: Here, we investigate metastatic variation seen clinically in patients with PDAC and murine PDAC tumors and identify MYC as a major driver of this heterogeneity.

INTRODUCTION

Tumor heterogeneity, most commonly studied in a primary disease setting, is a critical driver of phenotypic diversity, culminating in metastatic, lethal cancers (1–5). In most cancers, prognosis and therapeutic decisions are defined by the presence or absence of metastasis. However, tumor heterogeneity is increasingly being questioned at the level of metastatic disease, with recent studies in several cancer types suggesting that metastasis is not a binary phenotype but rather a disease spectrum ranging from oligometastatic (limited) to polymetastatic (widespread) disesase (6–8). Heterogeneity in the manifestation of metastatic disease can guide decisions on the use of local–regional versus systemic therapies with emerging evidence of its importance in clinical outcome (9–11). Despite its clinical significance, the mechanisms that underlie this spectrum of metastatic states remain unclear and largely understudied.

Pancreatic ductal adenocarcinoma (PDAC) represents a disease entity well suited for the study of metastasis, as most PDACs present with metastatic disease that is associated with a dismal prognosis (12). Genomic studies have comprehensively cataloged core mutations responsible for primary tumor development in PDAC (e.g., *KRAS*, *TRP53*, *CDKN2A*, and *SMAD4*), paving the path for genomic investigations of metastatic disease and the identification of metastasis-promoting alterations. Indeed, recent sequencing studies and functional analysis in model systems have associated genomic amplification in mutant *KRAS* alleles with progression from the nonmetastatic (stage III) to metastatic (stage IV) disease state (13). However, genetic factors mediating metastasic heterogeneity in patients and, importantly, the downstream cellular mechanisms remain largely undefined (14–18). Furthermore, it is unclear whether metastasis-associated alterations perturb the tumor microenvironment, whose influence on metastatic behavior is well documented

[1]Department of Internal Medicine and Children's Research Institute, UT Southwestern Medical Center, Dallas, Texas. [2]Harold C. Simmons Comprehensive Cancer Center, UT Southwestern Medical Center, Dallas, Texas. [3]Division of Gastroenterology, Department of Medicine, Penn Pancreatic Cancer Research Center and Abramson Family Cancer Research Institute, University of Pennsylvania, Philadelphia, Pennsylvania. [4]Cancer Biology and Genetics Program, Sloan Kettering Institute, New York, New York. [5]Division of Oncology and Center for Childhood Cancer Research, Children's Hospital of Philadelphia, Philadelphia, Pennsylvania. [6]Department of Biomedical and Health informatics and Center for Data-Driven Discovery in Biomedicine, Children's Hospital of Philadelphia, Philadelphia, Pennsylvania. [7]PanCuRx Translational Research Initiative, Ontario Institute for Cancer Research, Toronto, Ontario, Canada. [8]Department of Surgery, Montefiore Medical Center, Albert Einstein College of Medicine, Bronx, New York. [9]Department of Radiation Oncology, University of Pennsylvania, Philadelphia, Pennsylvania. [10]Department of Surgery, Hospital of the University of Pennsylvania, Philadelphia, Pennsylvania. [11]The David M. Rubenstein Center for Pancreatic Cancer Research, Human Oncology and Pathogenesis Program, Memorial Sloan Kettering Cancer Center, New York, New York. [12]Division of Hematology/Oncology, Department of Medicine, University of Pennsylvania, Philadelphia, Pennsylvania. [13]Department of Pathology, Montefiore Medical Center, Albert Einstein College of Medicine, Bronx, New York. [14]Department of Pathology, Memorial Sloan Kettering Cancer Center, New York, New York. [15]Princess Margaret Cancer Centre, Toronto, Ontario, Canada. [16]Department of Medical Biophysics, University of Toronto, Toronto, Ontario, Canada. [17]Division of Gastroenterology, Department of Medicine, University of Pennsylvania, Philadelphia, Pennsylvania.

R. Maddipati, R.J. Norgard, and T. Baslan contributed equally to this article.

Corresponding Authors: Ravikanth Maddipati, UT Southwestern Medical Center, 5323 Harry Hines Boulevard, J05.142, Dallas, TX 75390. Phone: 734-834-5546; E-mail: Ravikanth.Maddipati@UTsouthwestern.edu; and Ben Z. Stanger, University of Pennsylvania Perelman School of Medicine, 421 Curie Boulevard, Philadelphia, PA 19104. Phone: 215-746-5560; E-mail: bstanger@upenn.edu

Cancer Discov 2022;12:542–61

doi: 10.1158/2159-8290.CD-20-1826

(19–31). Therefore, understanding the interplay between genetic alterations that influence metastatic behavior and the tumor biology that promotes it—via cell-autonomous and/or non–cell-autonomous mechanisms—is crucial for understanding metastasis as a distinct disease state and critical for the development of more effective treatments.

One barrier to understanding metastatic heterogeneity has been a paucity of model systems that capture this natural variation and allow for direct assessments of paired primary tumors and metastases *in vivo*. This has limited the ability to define factors intrinsic to primary tumors that influence the extent of metastatic spread. We previously developed an autochthonous model of PDAC—the KPCX model—that employs multiplexed fluorescence-based labeling to track the simultaneous development of multiple primary tumor cell lineages and follow them as they metastasize (32). Importantly, this technique facilitates confirmation of lineage relationships *in vivo*, such that primary tumor clones with substantial metastatic potential can be distinguished from those having poor metastatic potential. Here, we show that this system recapitulates the variation in metastatic burden found in human PDAC, and we use it to dissect molecular and cellular features contributing to metastatic heterogeneity.

RESULTS

Metastatic Burden Is Variable in Human and Murine PDAC

Although most patients with PDAC have metastases (principally liver and lung), the number of metastases is highly variable from patient to patient (33, 34). Importantly, data regarding metastases have largely been obtained at autopsy and thus are confounded by varying treatment histories and reseeding due to end-stage disease (4). Thus, we first sought to characterize the burden of metastases in treatment-naive patients. To this end, we performed a retrospective analysis of initial computed tomography (CT) scans from 55 patients newly diagnosed with metastatic (stage IV) PDAC (Fig. 1A). The total number of lesions in the lung and liver was counted by examining both coronal and sagittal planes for both organs and binned into groups of 10, revealing a wide distribution of metastatic burden (Fig. 1B). K-means clustering identified two metastatic subgroups: a Met^{Low} subgroup (≤10 metastases, 25/55) and a Met^{High} subgroup (>10 metastases, 30/55; Fig. 1B; Supplementary Fig. S1A). Primary tumor size, age, sex, and race were not correlated with differences in metastatic burden (Fig. 1C; Supplementary Fig. S1B). However, having a greater number of metastases was associated with worse overall survival (Fig. 1D). Thus, even among patients with stage IV PDAC, metastatic burden is variable and correlates with clinical outcome.

We hypothesized that the differences in metastatic burden seen in human PDAC may also be present in autochthonous murine models. To test this, we used the KPCXY model—in which **C**re-mediated recombination triggers expression of mutant *Kras*^{G12D} and deletion of one allele of *Trp53* in the pancreatic epithelium along with **Y**FP and confetti (**X**) lineage tracers (Fig. 1E; Methods)—to measure metastatic heterogeneity in a cohort of tumor-bearing mice. By exploiting the multicolor features of the KPCX model, we previously showed that these mice harbor (on average) two to five independent primary tumor clones; importantly, the clonal marking of tumors with different fluorophores makes it possible to infer the lineages of primary tumors with different metastatic potential (32). In our earlier work with this model, we noted that in most tumor-bearing animals, even those with multiple primary tumors, liver and lung metastases were driven by a single tumor clone (Fig. 1E; Supplementary Fig. S1C). This suggested that tumor cell–intrinsic factors strongly influence the metastatic behavior of a tumor, even within a single animal.

To quantify differences in metastatic burden, we examined a panel of mice with at least two uniquely labeled fluorescent tumors in which most metastases could be attributed to a specific tumor on the basis of color (Fig. 1E; Supplementary Fig. S1C). A total of 85 primary tumors from 30 mice were examined, and gross metastases to the liver and lung arising from each tumor were then quantified by stereomicroscopy (Methods). Murine PDACs exhibited a wide distribution of metastatic burden, with a pattern resembling that of the human disease (Fig. 1F). Similarly, K-means clustering grouped murine samples into a low-metastasis subgroup (≤10 metastases, 58/85) and a high-metastasis subgroup (>10 metastases, 27/85), which we similarly refer to as Met^{Low} and Met^{High}, respectively (Fig. 1F; Supplementary Fig. S1D). As with the human disease, neither primary tumor size nor tumor cell proliferation correlated with metastatic burden (Fig. 1G; Supplementary Fig. S1E). Thus, the KPCXY model recapitulates the intertumoral metastatic heterogeneity seen in human PDAC and provides a unique experimental model for comparing highly metastatic and poorly metastatic tumor clones.

Individual Tumor Lineages in KPCXY Mice Correspond to Clones with Distinct Somatic Copy-Number Profiles

Although primary KPCXY tumors were easily distinguishable based on the expression of a distinct fluorophore, each tumor could have arisen via the clonal expansion of a single cell or through fusion of multiple tumors that happened to share the same color. Somatic copy-number alterations (SCNA) have been shown to provide an unambiguous picture of genomic heterogeneity and lineage relationships between primary tumors and matching metastases in human disease (35). Consequently, we performed copy-number analysis via genome sequencing on a set of 20 primary tumors, including multiregional sampling on a subset of the tumors in which sufficient tissue was available (nine tumors with two to four regions sampled per tumor; Fig. 2A; Supplementary Table S1). Tumors bearing different colors exhibited unique DNA copy-number profiles, indicating that they arose independently (Fig. 2B; Supplementary Fig. S2A; ref. 36). By contrast, multiregional sampling of monochromatic tumors revealed shared copy-number alterations, indicating that all subregions within a given tumor (defined by color) shared a common ancestral lineage (Fig. 2C; Supplementary Fig. S2B). In addition, subregion-specific alterations were also observed, suggesting that subclonal heterogeneity is also present in each tumor (Fig. 2C; Supplementary Fig. S2B). These results

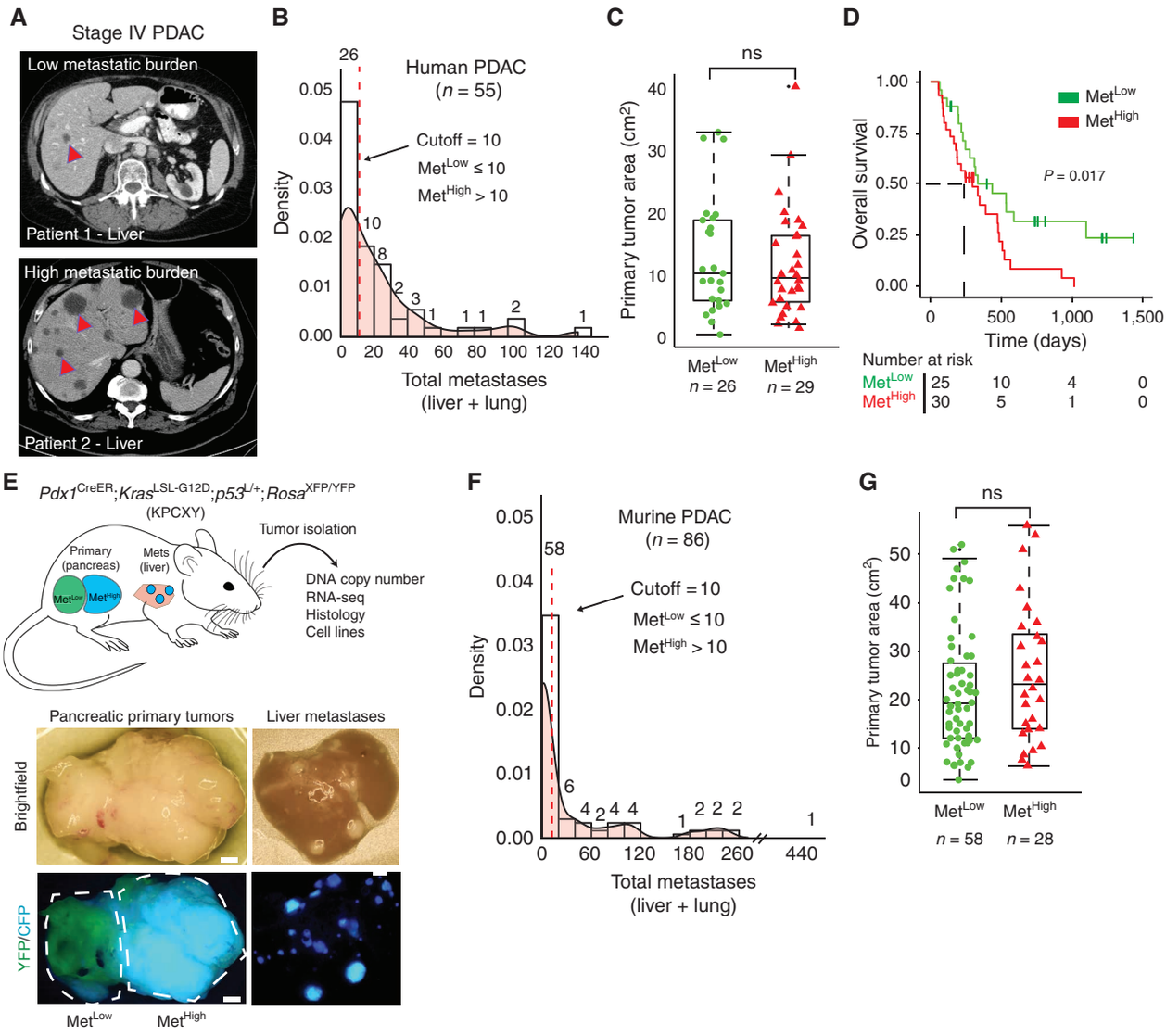

Figure 1. Advanced pancreatic tumors exhibit intertumoral differences in their propensity for metastasis. **A,** CT imaging of human PDAC liver metastasis demonstrating heterogeneity in metastatic burden in stage IV disease. Arrowheads indicate solitary metastasis in the top image and selected metastases in the bottom. **B,** Density plot and histogram showing the distribution of total (liver and lung) metastases enumerated from CT scans of human stage IV PDAC at the time of diagnosis ($n = 55$). Values above each histogram bar represent the number of patients in each group. The vertical dotted line (red) represents the cutoff between Met^{Low} tumors [≤10 metastases (mets)] and Met^{High} tumors (>10 mets) determined by k-means clustering. **C,** Quantification of tumor area (based on tumor dimensions from largest cross-sectional plane on imaging) comparing Met^{Low} and Met^{High} cases from the cohort in **B**. **D,** Overall survival analysis of the cohort in **B**. **E,** Top, schematic view of the KPCXY model, showing multiple primary tumors distinguishable by color arising in the pancreas with matched metastases in the liver. Bottom, representative fluorescent stereomicroscopic images showing a YFP$^+$ tumor adjoining a CFP$^+$ tumor in the pancreas (left) and liver metastases derived from the CFP$^+$ tumor in the same animal (right). **F,** Density plot and histogram showing the distribution of total (liver and lung) metastases enumerated at autopsy of KPCXY mice. Values above each histogram bar represent the number of tumors giving rise to the indicated number of metastases, based on color ($n = 85$ tumors from 30 KPCXY mice). The vertical dotted line (red) represents the cutoff between Met^{Low} tumors (≤10 mets, $n = 58$) and Met^{High} tumors (>10 mets, $n = 28$) determined by k-means clustering. **G,** Quantification of tumor area comparing Met^{Low} and Met^{High} tumors from the cohort in **F**. Statistical analysis by Student unpaired *t* test with *P* values indicated (ns, not significant). Box-and-whisker plots in **C** and **G** indicate mean and interquartile range. Scale bar for **E**, 1 mm.

suggest that the monochromatic tumors observed in KPCXY mice are clonal in origin and continue to undergo subclonal evolution during tumor progression.

To ascertain the lineage relationships between primary tumors and metastases, we compared DNA copy-number profiles between liver metastases and primary tumors within a given mouse. This revealed that primary tumors and metastases of the same color shared common DNA copy-number profiles across the dataset, confirming on a genetic basis the fluorescence-based lineage relationships (Fig. 2D–F; Supplementary Fig. S2C). As most lung metastases were microscopic and difficult to isolate by dissection, they were not included in the molecular analysis. Together, these results indicate that the lineage history of metastases

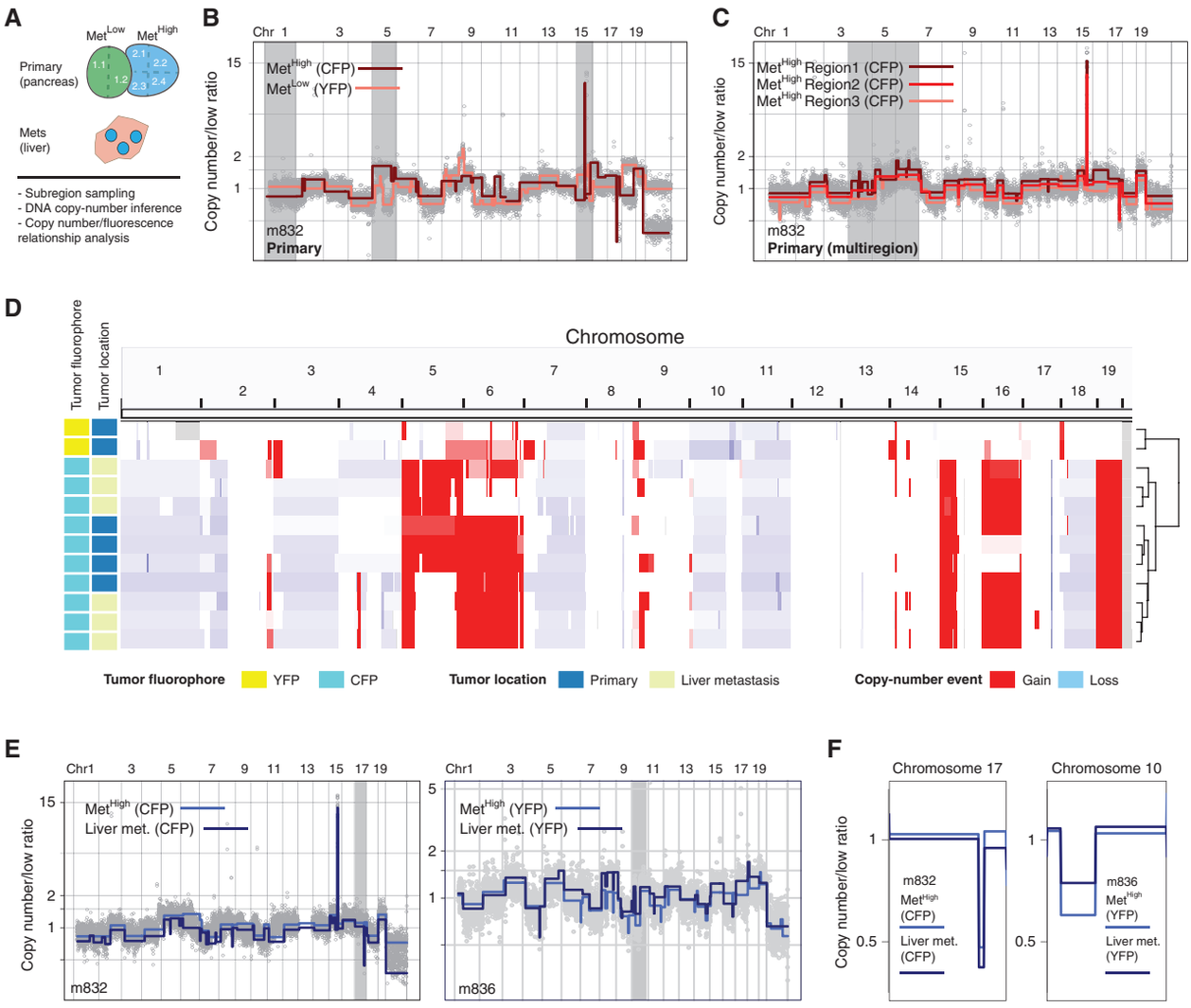

Figure 2. SCNA analysis confirms fluorescence-based lineage relationships and reveals genetic heterogeneity in paired primary pancreatic tumors and liver metastases. **A,** Schematic representation of KPCXY pancreatic tumor and matching liver metastases with multiregion sampling for copy-number sequence analysis. **B,** Representative genome-wide copy-number profiles of Met^{High} (CFP$^+$ fluorescence) and Met^{Low} (YFP$^+$ fluorescence) tumors from mouse 832 (m832) as depicted in Fig. 1E. Gray shading denotes alterations that are unique to the Met^{High} (CFP$^+$) tumor. The *y*-axis illustrates normalized read count values (low ratio), which are directly proportional to genome copy number at a given chromosomal location. The copy-number profiles are centered around a mean of 1 with gains and deletions called for segments with values higher and lower than the mean, respectively (Methods). **C,** Representative genome-wide copy-number profiles of three subsampled tissue regions of the Met^{High} (CFP$^+$) primary tumor from m832. Gray shading denotes alterations that are found heterogeneously from multiregion sequencing of the primary tumor. **D,** Genome-wide heat map with hierarchical clustering based on copy-number alterations of matched primary and metastatic samples profiled from m832. **E,** Representative genome-wide copy-number profiles of fluorescently matched primary and metastatic tissue from two profiled mice (m832, left; m836, right), illustrating the shared clonal genetic lineage. **F,** Zoomed-in chromosomal views of copy-number alterations with distinguishing breakpoint patterns supporting shared genetic lineage. Panels are ordered as in **E**.

can be inferred by color and genomic analysis, allowing primary tumors with high versus low metastatic potential to be unambiguously classified.

Genomic and Transcriptional Analyses Identify *Myc* as a Potential Driver of Metastatic Phenotypes

We next sought to examine the molecular differences that distinguish primary tumors with high versus low metastatic potential. We began by examining large-scale (mega-base level as well as chromosome-wide) SCNAs in 20 Met^{High} and Met^{Low} primary tumor samples. This analysis revealed largely similar genome-wide copy-number patterns between Met^{High} and Met^{Low} primary tumors, with key PDAC-associated genes, such as loss of heterozygosity at *Cdkn2a/b* and *Trp53* as well as chromosomal gain of *Kras* occurring at similar frequencies (Supplementary Fig. S3A). Thus, KPCXY tumors exhibit frequent copy-number alterations in canonical PDAC genes, but these alterations do not account for the variation in metastatic behavior between Met^{High} and Met^{Low} tumors.

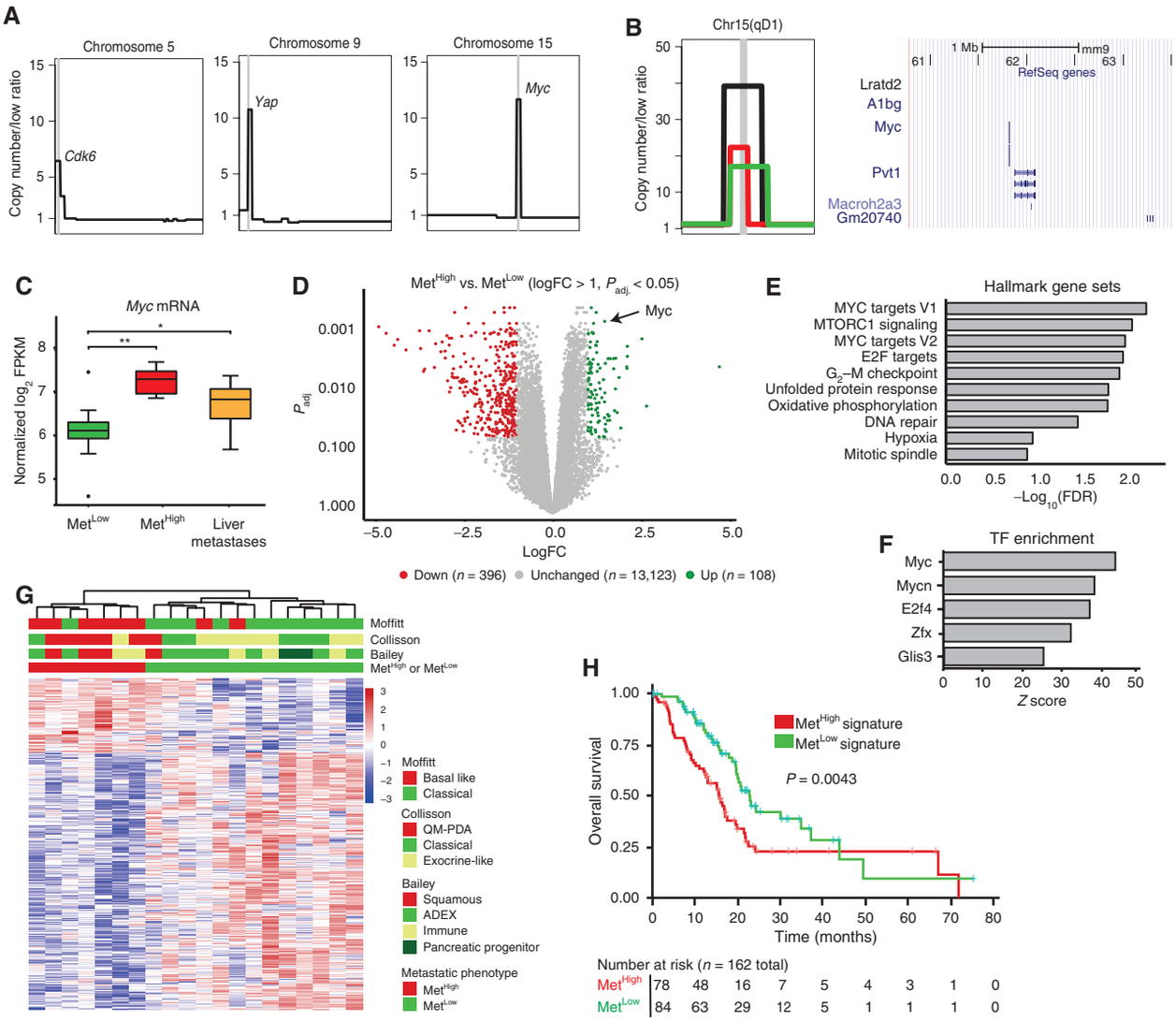

Figure 3. The Met^{High} phenotype is associated with focal, high-amplitude *Myc* amplifications and elevated expression. **A,** Schematic representation of focal amplifications identified in profiled primary tumors. Vertical gray line denotes the location of amplicon and likely driver gene. **B,** Zoomed-in schematic representation of three identified *Myc* amplicons in Met^{High} tumors illustrating the focal and high-amplitude nature of the event (left). Each event (amplicon) is illustrated by a different colored segment line. The shared amplified region between the different amplicons is denoted by the chromosomal cytoband top of panel and illustrated in a UCSC Genome Browser view (right) with RefSeq genes, including *Myc*, illustrated. **C,** Box-and-whisker plot showing *Myc* mRNA levels in Met^{High} tumors ($n = 7$) and paired metastases ($n = 34$) compared with Met^{Low} tumors ($n = 13$). FPKM, fragments per kilobase of exon per million. **D,** Volcano plot illustrating genes meeting cutoffs for differential expression [log fold change (logFC) >1, $P_{adj.} < 0.05$] between Met^{High} and Met^{Low} tumors ($n = 20$ tumors used in the comparison). Genes upregulated in Met^{High} tumors are highlighted in green, and genes upregulated in Met^{Low} tumors are highlighted in red. **E,** Top 10 hallmark gene sets identified as enriched in Met^{High} tumors compared with Met^{Low} tumors using all differentially expressed genes (DEG; $P_{adj.} < 0.05$). **F,** Top five transcription factor (TF) binding sites enriched in DEGs in Met^{High} tumors compared with Met^{Low} tumors ($P_{adj.} < 0.05$) identified by Metacore prediction software. **G,** Heat map showing unsupervised clustering of DEGs (logFC >1, $P_{adj.} < 0.05$) between Met^{High} and Met^{Low} tumors ($n = 20$) and their association with PDAC transcriptional subtypes previously reported by Collisson and colleagues (42), Moffitt and colleagues (15), and Bailey and colleagues (16). ADEX, aberrantly differentiated endocrine exocrine; QM-PDA, quasi-mesenchymal-pancreatic ductal adenocarcinoma. **H,** Kaplan–Meier analysis showing overall survival of patients with PDAC in the TCGA cohort stratified into those with a Met^{High} signature (red line) versus those with a Met^{Low} signature (green line). Signature based on DEGs with absolute logFC >0.58 and $P_{adj.} < 0.05$ (736 up- and 1,036 downregulated genes). Statistical analysis in **C** was performed by Wilcoxon test (*, $P = 3.9 \times 10^{-4}$; **, $P = 5.3 \times 10^{-5}$). Box and whiskers represent median mRNA expression and interquartile range. Statistical analysis in **H** was performed by log-rank test.

We next asked whether other factors (genomic and/or transcriptional) may be acting to enhance metastasis in the Met^{High} group. Focal amplifications in driver oncogenes—*Cdk6* and *Yap* in breast cancer and mutant *Kras* in PDAC—have been linked to the acquisition of metastatic competence (13, 14, 37, 38). Consistent with prior studies, we observed focal amplicons at genomic regions encoding *Cdk6*, *Yap*, and *Kras* in our tumors (Fig. 3A; Supplementary Fig. S3A; refs. 13, 14, 37–39). However, in contrast to these amplifications, which occurred at equal frequencies in Met^{High} and Met^{Low} tumors, focal

high-amplitude amplifications in *Myc* were found in 42.8% (3/7) of Met^{High} tumors compared with 7.6% (1/13) of Met^{Low} tumors (Fig. 3B). Thus, *Myc* amplifications are enriched in Met^{High} tumors. In all cases, these amplifications were maintained in paired metastases (Supplementary Fig. S3B). In addition, RNA sequencing (RNA-seq) analysis demonstrated significantly higher levels of *Myc* transcripts in Met^{High} tumors and metastases compared with Met^{Low} tumors (Fig. 3C); overall, *Myc* was the third-most significantly upregulated gene in Met^{High} tumors compared with Met^{Low} tumors (Fig. 3D). Gene set enrichment analysis (GSEA) of the differentially expressed genes between Met^{High} and Met^{Low} tumors identified MYC and E2F signatures as highly enriched, along with other signatures that have been implicated in PDAC metastasis, including unfolded protein response, oxidative phosphorylation, and hypoxia (Fig. 3E; Supplementary Table S2; refs. 31, 40, 41). Moreover, MetaCore transcription factor enrichment analysis identified MYC as the transcription factor most significantly associated with genes overexpressed in Met^{High} tumors (Fig. 3F), and Ingenuity Pathway Analysis placed *Myc* at the center of the interactome generated by these differentially expressed genes (Supplementary Fig. S4). Collectively, these results demonstrate a strong association between a tumor's metastatic behavior and the abundance and/or activity of MYC at the genomic and transcriptional levels.

Human PDAC can be grouped into two main transcriptomic subtypes—a well-differentiated classical/exocrine-like/progenitor (classical) subtype and a poorly differentiated squamous/quasi-mesenchymal/basal (basal-like) subtype (15, 16, 18, 42). We found that Met^{High} tumors were associated with basal-like PDACs, in line with their more aggressive behavior (Fig. 3G). Likewise, applying murine Met^{Low} and Met^{High} signatures (see Methods) to human data from The Cancer Genome Atlas (TCGA) predicted a worse survival—indicative of disease recurrence—for patients with a Met^{High} signature (Fig. 3H). These data indicate that murine Met^{High} tumors correspond to the more aggressive subtypes of human PDAC.

A Panel of Cell Lines that Preserve the Met^{Low} and Met^{High} Phenotypes

To understand the mechanisms underlying these different metastatic properties, we generated a panel of cell lines from six Met^{High} tumors and five Met^{Low} tumors. Consistent with the parental *in vivo* tumors, *Myc* gene expression and MYC protein levels were higher in the Met^{High} lines compared with the Met^{Low} lines (Fig. 4A and B). SCNA analysis in these cells lines found that they retained most of the genomic alterations found in the matched primary samples, including *Myc* amplifications (Supplementary Fig. S5A and S5B). Furthermore, *Myc* amplifications were not found in any of the cell lines whose tumors were originally characterized as non–*Myc* amplified, indicating that *in vitro* culture does not select for this specific copy-number alteration. Importantly, elevations in MYC mRNA and protein were observed in both the *Myc*-amplified and nonamplified Met^{High} lines, suggesting that elevated MYC expression is a stable phenotype of these cells in culture.

To investigate the metastatic properties of the Met^{High} and Met^{Low} lines *in vivo*, we performed orthotopic implantation of five Met^{High} and five Met^{Low} lines into the pancreas of NOD.SCID mice and examined distant organs for evidence of metastasis. Although the weights of Met^{High} and Met^{Low} tumors were not significantly different (Supplementary Fig. S6A), Met^{High} tumors gave rise to 28-fold more liver and lung metastases compared with Met^{Low} tumors (Fig. 4C). Consistent with the cell line expression differences, the orthotopic Met^{High} tumors expressed higher levels of *Myc* compared with Met^{Low} tumors (Supplementary Fig. S6B). To further confirm that differences in *Myc* expression were sufficient to drive the metastatic phenotype, we introduced a *Myc* overexpression (Myc_OE) construct into four Met^{Low} lines and generated orthotopic tumors (Supplementary Fig. S6C). *Myc* overexpression led to a dramatic (22-fold) increase in liver and lung metastases (Fig. 4D). Thus, cell lines derived from spontaneously generated Met^{High} and Met^{Low} tumors retain their metastatic phenotypes upon implantation.

MYC Promotes Tumor Cell Intravasation through the Recruitment of Tumor-Associated Macrophages

To form distant metastases, cancer cells must navigate a series of events collectively referred to as the "metastatic cascade." These events include (i) intravasation into the bloodstream or lymphatics, (ii) survival in the circulation, (iii) extravasation from the vessel, and (iv) growth and survival at the distant site (43). To determine the step(s) at which MYC was exerting its prometastatic effects, we began by measuring the number of circulating tumor cells (CTC) in orthotopically implanted Met^{High} and Met^{Low} tumors and in Met^{Low} tumors engineered to overexpress *Myc*. Remarkably, CTCs arising from Met^{High} and Myc_OE tumors were 38-fold and 17-fold more abundant than those arising from Met^{Low} tumors (Fig. 4E), far greater than the approximately twofold increase in tumor weight resulting from *Myc* overexpression (Supplementary Fig. S6D). Next, we performed a tail vein metastasis assay, which bypasses the invasion step by introducing tumor cells directly into the bloodstream, and measured lung metastases. Surprisingly, in contrast to the orthotopic tumor experiment, there was no difference in the number of metastases between Met^{High} and Met^{Low} lines (Fig. 4F). Moreover, *Myc* overexpression had no effect on tumor cell survival in the circulation (Supplementary Fig. S6E–S6G). Taken together, these data suggest that Met^{High} tumors achieve a higher metastatic rate principally by promoting cancer cell invasion into the circulation, which can be driven by increased *Myc* expression.

Beyond activation of tumor cell intrinsic programs, MYC can also affect tumor phenotypes by altering the tumor immune microenvironment (TiME; refs. 44–46). Thus, we sought to determine if differences in MYC levels between Met^{High} and Met^{Low} tumors were associated with distinct TiMEs. To this end, we examined the immune composition of parental primary tumors by staining for markers of immune cells previously implicated in metastasis of PDAC and other cancers. Although Met^{High} and Met^{Low} tumors had a similar degree of neutrophil infiltration, Met^{High} tumors had lower numbers of CD3^{+} T cells but were highly enriched for F4/80^{+} macrophages (Fig. 5A). Thus, compared with Met^{Low} tumors, the TiME of Met^{High} tumors contains an increased number of tumor-associated macrophages (TAM).

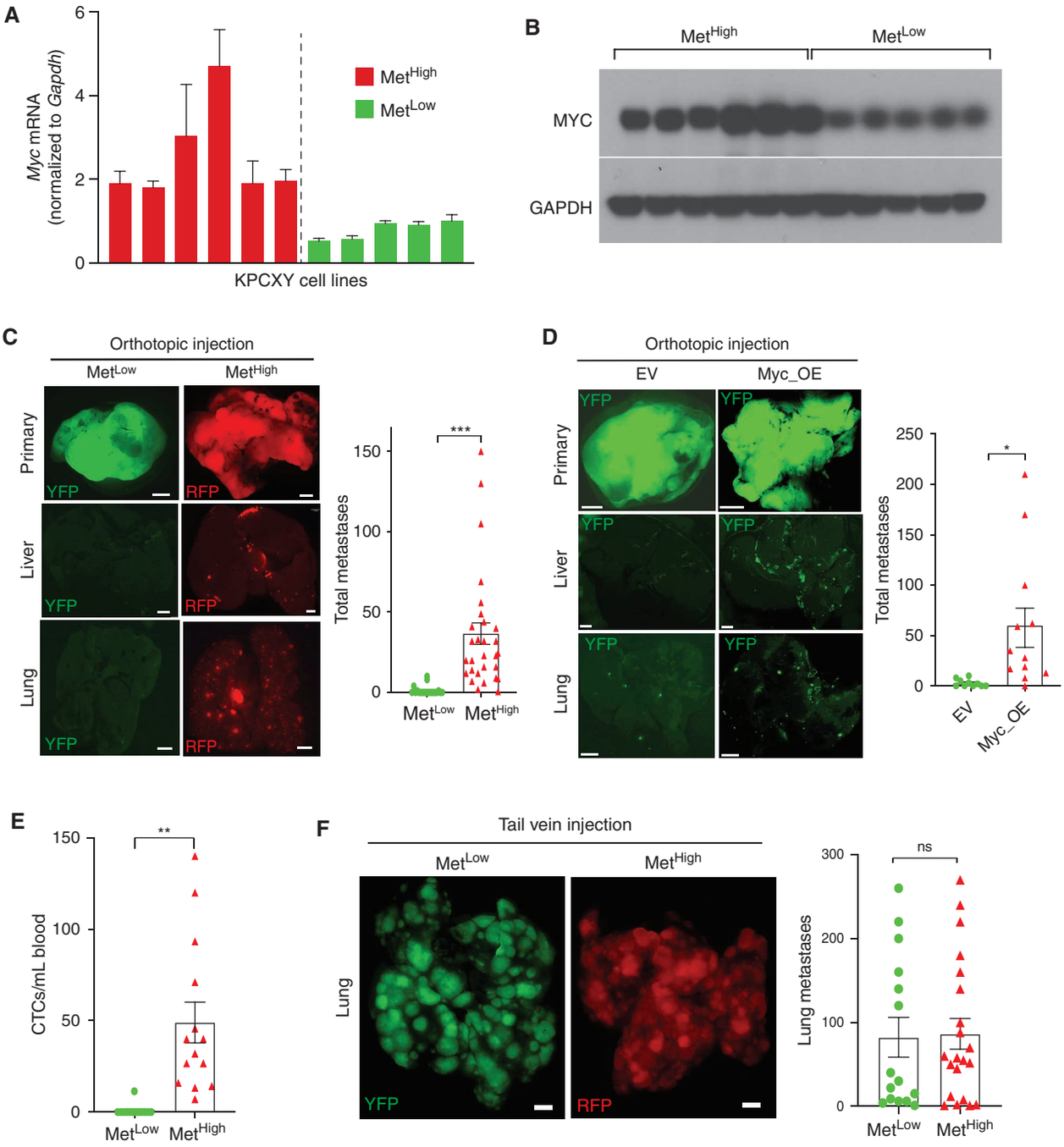

Figure 4. MYC regulates metastasis by enhancing tumor cell intravasation. **A,** Bar graph showing *Myc* mRNA levels in cell lines derived from Met^{High} and Met^{Low} tumors, normalized to Gapdh ($n = 6$ Met^{High} and $n = 5$ Met^{Low} cell lines). **B,** Western blot showing corresponding MYC protein levels in cell lines derived from Met^{High} and Met^{Low} tumors shown in **A**. **C,** Representative fluorescent images of primary tumors and associated liver and lung metastases following orthotopic transplantation of the cell lines in **A** and **B** into NOD.SCID mice. The bar graph shows the total number of metastases (liver and lung) counted following orthotopic transplantation of five Met^{Low} cell lines or five Met^{High} cell lines (pooled data from $n = 49$ mice in total). **D,** Representative fluorescent images of primary tumors, liver metastases, and lung metastases following orthotopic transplantation of Met^{Low} cell lines that were stably transduced with either a Myc_OE or an empty vector (EV) construct. The bar graph shows the total number of metastases (liver and lung) counted following orthotopic transplantations of Myc_OE or EV cells. Data were pooled from four independent Met^{Low} lines transduced with either the Myc_OE or EV construct transplanted into 12 NOD.SCID (for the Myc_OE cells) or 10 NOD.SCID mice (for the EV cells). **E,** Quantification of CTCs in arterial blood derived from the orthotopic tumors depicted in **C** ($n = 27$ mice examined) and **D** ($n = 12$ mice examined). **F,** Representative fluorescent images of lung metastases following tail vein injection of cell lines derived from the Met^{Low} and Met^{High} primary tumor clones. The bar graph shows the total number of lung metastases counted following tail vein injection of five Met^{Low} cell lines or five Met^{High} cell lines (pooled data from $n = 36$ mice in total). Statistical analysis by Student unpaired *t* test with significance indicated (*, $P = 0.0152$; **, $P = 0.013$; ***, $P = 0.0008$; ns, not significant). Error bars indicate SEM (**C**–**F**). Scale bar, 1 mm (**C**, **D**, and **F**).

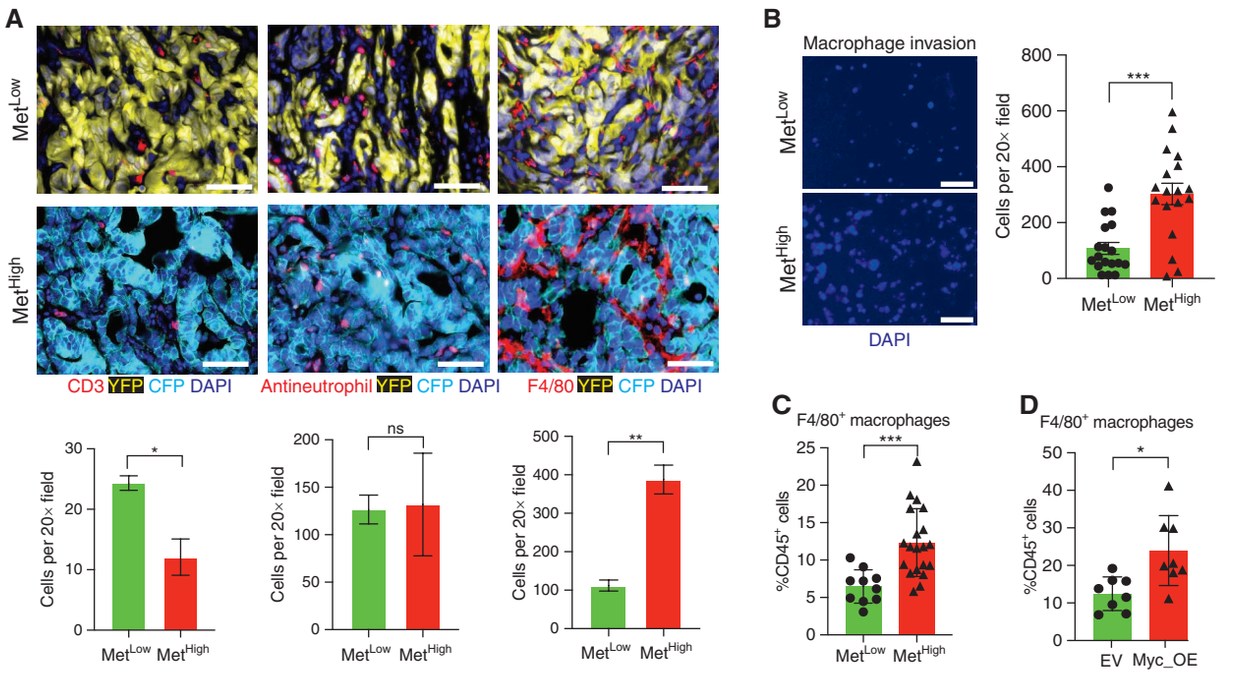

Figure 5. MYC recruits prometastatic macrophages to the tumor microenvironment. **A,** Representative immunofluorescence images (top) and quantification (bottom) of T cells (CD3$^+$), neutrophils (antineutrophil antibody$^+$), and macrophages (F4/80$^+$) in primary KPCXY tumors categorized as Met^{Low} or Met^{High}, with quantification below ($n = 3$ mice for each subgroup and four to five random fields of view analyzed). **B,** Representative immunofluorescence images (left) and quantification (right) of macrophages that have migrated across a transwell filter following coculture with Met^{High} or Met^{Low} tumor cells ($n = 2$ Met^{Low} and $n = 2$ Met^{High} cell lines used; three replicates per cell line with three 20× images taken per transwell; each dot represents quantification of an independent image). **C,** Quantification of tumor-infiltrating macrophages (as a percentage of total CD45$^+$ cells) in Met^{Low} or Met^{High} subcutaneous tumors assessed by flow cytometry ($n = 5$ Met^{High} cell lines and $n = 3$ Met^{Low} cell lines; two NOD.SCID mice examined per cell line with two tumors per mouse; each dot represents an independent tumor). **D,** Quantification of tumor-infiltrating macrophages (as a percentage of total CD45$^+$ cells) in Myc_OE or control (EV) subcutaneous tumors assessed by flow cytometry ($n = 2$ Myc_OE cell lines and $n = 2$ EV cell lines; two NOD.SCID mice examined per cell line with two tumors per mouse; each dot represents an independent tumor). (*continued on following page*)

To examine the ability of Met^{High} and Met^{Low} tumor cells to recruit macrophages, we cocultured these cell lines with primary bone marrow–derived murine macrophages (BMDM) in a transwell migration assay (39). Compared with Met^{Low} cocultures, Met^{High} cocultures exhibited greater macrophage migration toward the tumor cells (Fig. 5B). Consistent with these *in vitro* results, orthotopic tumors generated from Met^{High} cell lines exhibited greater TAM infiltration than those generated from Met^{Low} cell lines (Fig. 5C). Furthermore, Met^{Low} lines overexpressing *Myc* gave rise to tumors with greater TAM infiltration compared with controls (Fig. 5D). These results demonstrate that Met^{High} tumors exhibit enhanced macrophage recruitment and implicate *Myc* expression as a driver of macrophage infiltration. Macrophages have been reported to facilitate metastasis in several cancers (47). This is achieved, in part, through the activation of an "M2-like" polarization state in TAMs characterized by increased expression of ARG1 and CD206 expression (48). To determine whether *Myc* expression in pancreatic tumor cells alters macrophage phenotypes, we stained for these markers and found that both Met^{High} tumors and Myc_OE tumors were enriched for ARG1$^+$ and CD206$^+$ TAMs compared with Met^{Low} and EV control tumors (Fig. 5E–H). Thus, *Myc* overexpression is associated with an enrichment for M2-like macrophages in the tumor microenvironment.

In breast cancer, macrophages promote tumor cell invasion and metastasis through the development of specialized structures called tumor microenvironment of metastasis doorways, in which macrophages facilitate the movement of cancer cells across an endothelial barrier (49). To investigate whether macrophages might promote metastasis in PDAC through a similar mechanism, we performed an *in vitro* transendothelial migration (iTEM) assay, in which the proinvasive activity of *Myc* overexpression and macrophages could be directly assessed (50–52). Tumor cell intravasation across an endothelial monolayer was enhanced by either the addition of macrophages or *Myc* overexpression, an effect that was greatest when both stimuli were present (Fig. 5I).

To directly test whether TAMs are required for MYC-driven metastasis in PDAC, we performed a macrophage depletion experiment. We generated orthotopic tumors from Met^{Low} Myc_OE cells and 10 days later treated mice with a combination of the colony-stimulating factor receptor inhibitor GW2580 and liposomal clodronate (Fig. 5J). Consistent with prior studies (29, 53–55), this regimen was highly effective at depleting both circulating and tumor-resident macrophages (Supplementary Fig. S7A and S7B) and caused a modest increase in tumor weight (Supplementary Fig. S7C). Depeletion also reduced tissue-resident macrophages in liver and lung premetastatic niches with no significant effect on neutrophil

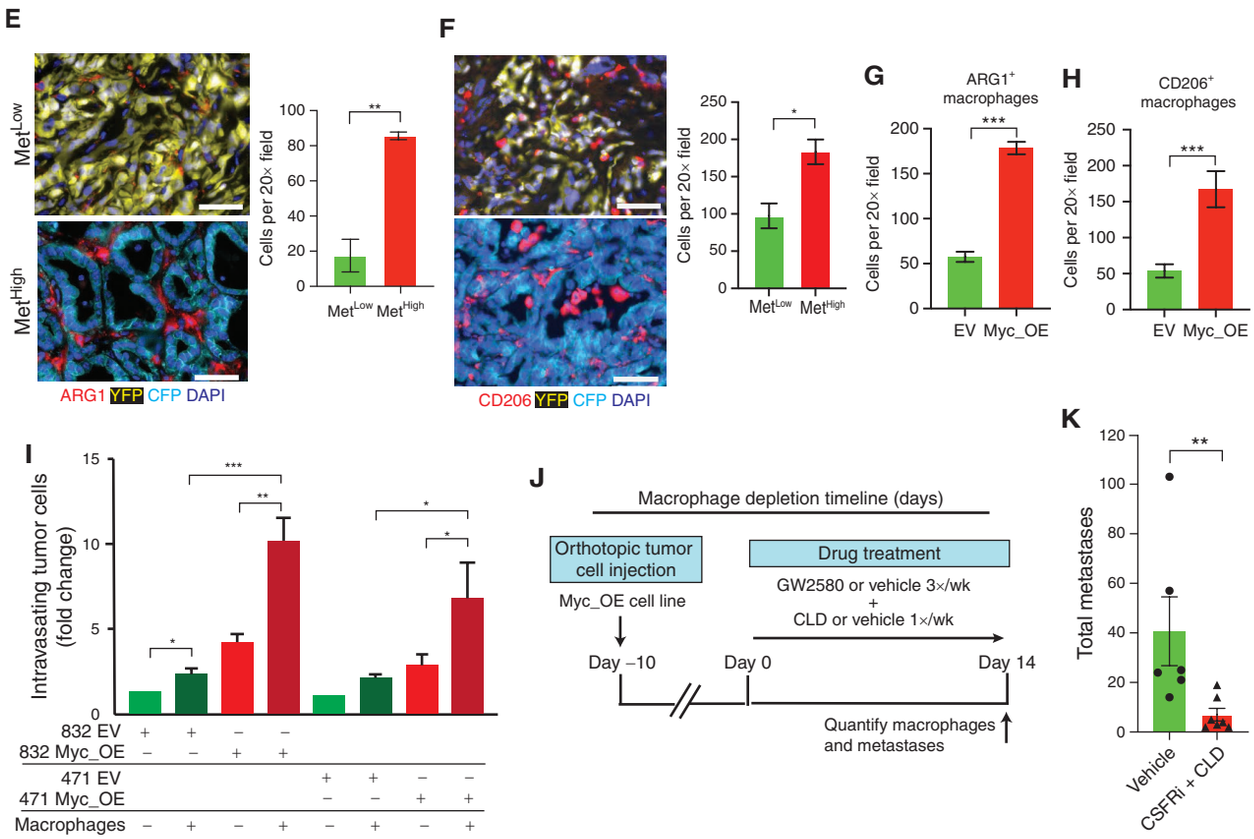

Figure 5. ***(Continued)*** **E** and **F,** Representative immunofluorescence images (left) and quantification (right) of ARG1$^+$ (**E**) and CD206$^+$ (**F**) TAMs in primary KPCXY tumors categorized as Met^{Low} or Met^{High} ($n = 3$ mice for each subgroup and four to five random fields of view analyzed). **G** and **H,** Quantification of ARG1$^+$ (**G**) and CD206$^+$ (**H**) TAMs in primary MYC_OE or control (EV) orthotopic tumors assessd by immunflourescence staining ($n = 2$ Myc_OE cell lines and $n = 2$ EV cell lines; two NOD.SCID mice examined per cell line; four to five random fields of view analyzed). **I,** Quantification of tumor cell intravasation from an iTEM assay. MYC_OE– or EV-transduced tumor cells were cultured in transwell filters seeded with an endothelial cell monolayer in the presence or absence of macrophages (see Methods). Tumor cells that traversed the endothelial layer were quantified and normalized to the EV control in the absence of macrophages for each of two Met^{Low} tumor lines. **J,** Schematic outline of the macrophage depletion experiment. Mice were orthotopically implanted with Myc_OE cells ($n = 2$ independent cell lines), and after 10 days, tumor-bearing animals were treated with a combination of colony-stimulating factor receptor inhibitor (CSFRi; GW2580) and liposomal clodronate (CLD) or vehicle. Metastases were quantified 14 days later. **K,** Quantification of total metastases (liver and lung) following the macrophage depletion strategy outlined in **J** ($n = 6$ control mice and $n = 7$ GW2580 + CLD mice; each dot represents an independent mouse). Statistical analysis (**A**–**H** and **K**) by Student unpaired *t* test with significance indicated (*, $P < 0.05$; **, $P < 0.005$; ***, $P < 0.0001$; ns, not significant); statistical analysis (**I**) by two-way ANOVA (*, $P < 0.05$; **, $P < 0.01$; ***, $P < 0.001$). Error bars indicate SEM. Scale bars, 10 μm (**A**, **E**, and **F**) and 50 μm (**B**).

abundance (Supplementary Fig. S7D–S7F). Macrophage depletion resulted in a four- to sixfold reduction in metastases (Fig. 5K), an effect that had no impact on CTC viability, seeding, or outgrowth in the lung (Supplementary Fig. S7G–S7J). Taken together, these data suggest that MYC enhances metastatic spread at least in part by creating a TAM-rich environment in the primary tumor that increases tumor cell invasion. Although previous studies have implicated macrophages in tumor cell infiltration, these results directly link this process to the genomic and transcriptional activation of MYC, which occurs naturally in our model and is subsequently selected for as a driver of metastasis (21, 26, 28, 47, 53, 56–61).

MYC Enhances TAM Recruitment and Metastasis through Increased Expression of CXCL3 and MIF

To identify factors that might be responsible for the increased abundance of macrophages in Met^{High} tumors, we mined our RNA-seq data to identify secreted factors that are differentially expressed between Met^{High} and Met^{Low} tumors [$P < 0.01$ and log fold change (logFC) >1]. This resulted in identification of six cytokines/chemokines upregulated in Met^{High} tumors (Supplementary Fig. S8A). Interestingly, each of these factors has been previously implicated in regulating macrophage recruitment in pancreatic and other cancer types (59, 62–65). To determine which of these factors may be regulated by MYC in a clinically relevant setting, we examined gene expression data from the COMPASS trial cohort of patients with PDAC, comparing tumors with either high or low levels of *MYC* expression. This revealed that three of the six factors (*MIF, CXCL3,* and *CCL3*) were also enriched in human PDACs exhibiting elevated *MYC* expression (Fig. 6A). To determine which of these factors depend on MYC for their expression, we used short hairpin RNA to knock down *Myc* levels in three Met^{High} tumor lines (Supplementary Fig. S8B).

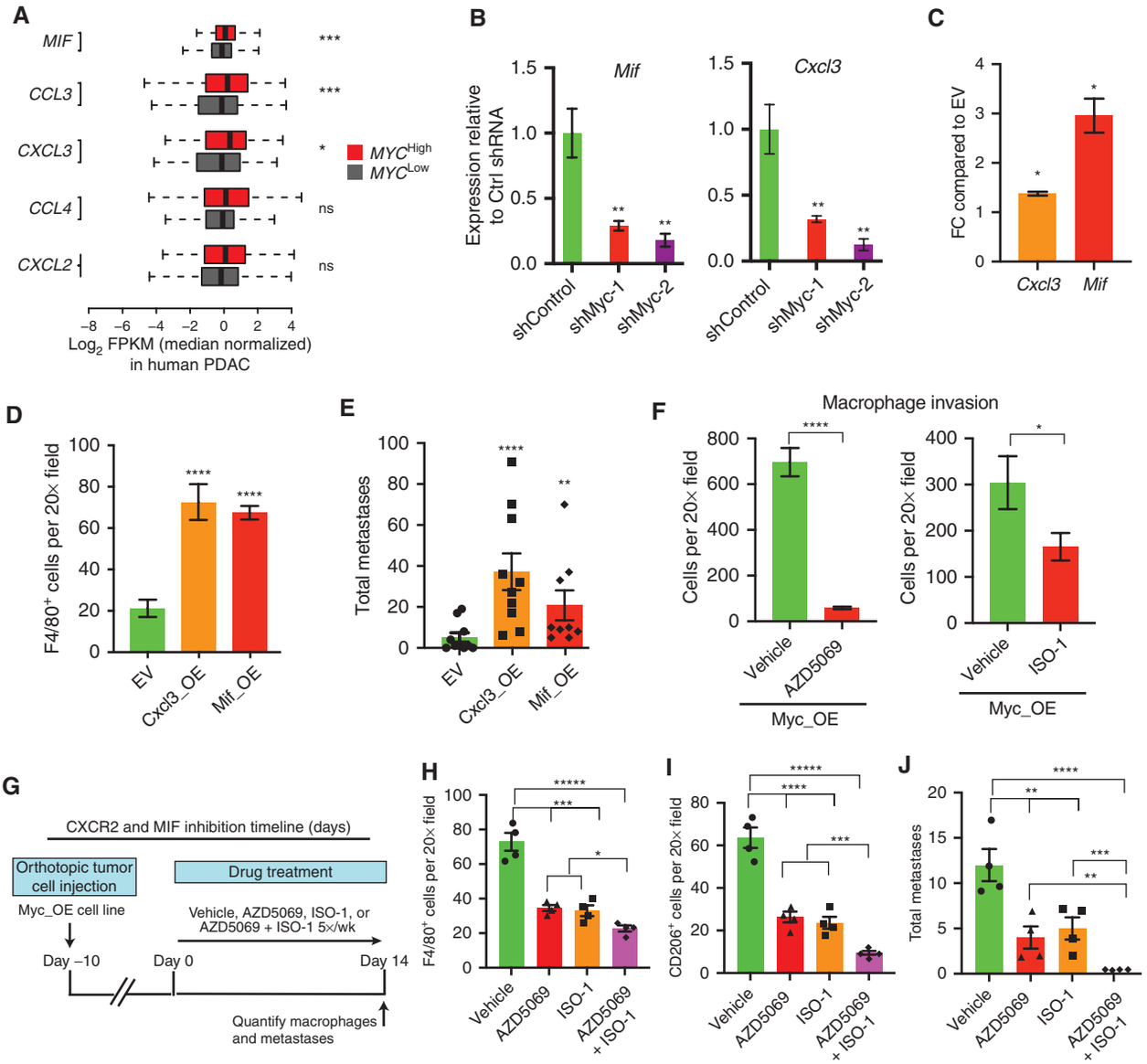

Figure 6. MYC acts through CXCL3 and MIF to promote macrophage recruitment and metastasis. **A,** Expression of selected cytokines/chemokines in human PDAC. Samples from the COMPASS cohort (enriched for tumor cells by laser capture microdissection) were stratified into *MYC*-high and *MYC*-low groups based on RNA-seq ($n = 373$) and assessed for the expression of five chemokines/cytokines identified as significantly upregulated in Met^{High} versus Met^{Low} tumors (Supplementary Fig. S8A). FPKM, fragments per kilobase of exon per million. **B,** Relative expression of *Mif* and *Cxcl3* in control or *Myc* knockdown [short hairpin RNA (shRNA)] Met^{High} cell line 850_Met^{High}_4. Data are representative of two independent Myc shRNAs ($n = 3$ biological replicates). **C,** Bar graph showing fold increase in *Cxcl3* and *Mif* mRNA levels comparing Myc_OE to EV control cell lines. Data are representative of two independent cell lines ($n = 3$ biological replicates). **D,** Quantification of total F4/80+ tumor-infiltrating macrophages by immunoflourescence in cell lines that were stably transduced with either a *Cxcl3* or *Mif* overexpression construct (Cxcl3_OE and Mif_OE, respectively) or empty vector (EV), with $n = 4$ tumors examined from each group with four to five random fields of view analyzed. **E,** Quantification of total metastases (liver and lung) following orthotopic transplantation of EV, Cxcl3_OE, or Mif_OE orthotopic tumors from **D**. Data were pooled from two independent Met^{Low} lines transduced with the Cxcl3_OE, Mif_OE, or EV construct transplanted into five NOD.SCID mice (for each cell line). Each dot represents an independent animal. **F,** Quantification of macrophages that migrated across a transwell filter following coculture with 832 Myc_OE tumor cells treated with either a CXCR2 inhibitor (AZD5069) or a MIF inhibitor (ISO-1). Data are representative of two independent experiments, including three replicates with four to five 20× images taken per transwell. **G,** Schematic outline of the CXCR2 and MIF inhibitor experiment. Mice were orthotopically implanted with 832 Myc_OE cells and after 10 days were treated with a CXCR2 inhibitor (AZD5069), MIF inhibitor (ISO-1), combination (AZD5069 + ISO-1), or vehicle. Metastases and macrophages were quantified 14 days later. **H** and **I,** Quantification of F4/80+ (**H**) and CD206 (**I**) macrophages in orthtotopic tumors following the CXCR2 and MIF strategy outlined in **G** ($n = 4$ tumors per group; four to five random fields of view analyzed; each dot represents an independent animal). **J,** Quantification of total metastases (liver and lung) following the CXCR2 and MIF strategy outlined in **G** ($n = 4$ control mice, $n = 4$ AZD5069 mice, $n = 4$ ISO-1 mice, and $n = 4$ AZD5069 + ISO-1 mice; each dot represents an independent animal). Statistical analysis by Student *t* test with significance indicated (*, $P < 0.05$; **, $P < 0.01$; ***, $P < 0.007$; ****, $P < 0.0005$; *****, $P < 0.0001$; ns, not significant). Error bars indicate SEM.

MIF and CXCL3 expression was significantly reduced following *Myc* knockdown (Fig. 6B), whereas the expression of the other factors was either unchanged or elevated following *Myc* knockdown (Supplementary Fig. S8C). Consistent with these findings, *Myc* overexpression in a Met^{Low} cell line resulted in the upregulation of these factors (Fig. 6C). Furthermore, analysis of the Gene Transcription Regulation Database and Eukaryotic Promoter Database revealed direct evidence for MYC binding to the *CXCL3* and *MIF* promoters (Supplementary Fig. S8D and S8E; refs. 66–69). These results suggest that MYC regulates macrophage recruitment in part through the regulation of MIF and CXCL3.

To further examine the role of these chemokines in macrophage recruitment, we overexpressed each factor in Met^{Low} lines (Supplementary Fig. S8F) and examined their effects *in vivo*. Compared with controls, orthotopic tumors from Cxcl3_OE and Mif_OE cells resulted in a three- to fourfold increase in intratumoral macrophages (Fig. 6D) and a significant increase in lung and liver metastases (Fig. 6E). Thus, CXCL3 and MIF overexpression is sufficient to increase TAM abundance and promote metastasis of Met^{Low} tumors.

Tumor-secreted factors can regulate immune cell phenotypes through specific recptor–ligand interactions and enzymatic activities. The cognate receptor for CXCL3 is CXCR2, which has previously been reported to modulate myeloid cell recruitment in prostate cancer and PDAC (59, 70). Similary, MIF can regulate immune cell function through binding various receptors and its tautomerase activity (71, 72). To examine the role of these factors in macrophage recruitment in our system, we treated Myc_OE tumor cells with a CXCR2 inhibitor (AZD5069) or MIF inhibitor (ISO-1) in an *in vitro* transwell migration assay (52, 70, 72, 73). Compared with vehicle controls, inhibition of CXCR2 or MIF led to a 2- to 10-fold decrease in macrophage migration (Fig. 6F). Next, we assessed the impact of these drugs on TAM recruitment and metastasis *in vivo* (Fig. 6G). Treatment of Myc_OE orthotopic tumors with AZD5069 or ISO-1 reduced TAM recruitment and metastatic burden (Fig. 6H–J) and caused a slight decrease in tumor weight (Supplementary Fig. S8G). Interestingly, compared with each inhibitor alone, the combination of both inhbitors resulted in significantly lower levels of TAMs ($F4/80^+$ and $CD206^+$) and metastasis (Fig. 6H–J). Taken together, these data suggest that multiple *Myc*-regulated factors contribute to macrophage recruitment and metastasis in PDAC.

Metastasis in Human PDAC Is Associated with *MYC* Gene Amplification and Elevated Expression

Given the finding that genomic and transcriptional variation in *Myc* was associated with metastatic heterogeneity in murine PDAC, we sought to determine whether *MYC* is associated with similar metastatic phenotypes in human PDAC. Because most PDAC samples in the International Cancer Genome Consortium (ICGC) and TCGA are derived from resected stage I/II tumors (18), these datasets provide limited insight into the determinants of metastatic burden. Consequently, we analyzed data from the COMPASS trial cohort (NCT02750657), which is focused on patients with metastatic PDAC and uses laser capture microdissection (LCM) to enrich for tumor cells prior to whole-genome sequencing (WGS) or RNA-seq (14, 74). By comparing primary tumors and metastases, we found that 11.3% (n = 17/133) of metastases were enriched for *MYC* amplifications compared with 1.61% (n = 4/244) of resectable tumors (Fig. 7A and B; P = 7.6e-5, Fisher test). Likewise, advanced tumors (defined as either locally advanced or metastatic) were significantly enriched for *MYC* amplifications (9.22%; n = 19/206) compared with resectable tumors having no evidence of metastasis at diagnosis (1.04%; n = 2/192; Supplementary Fig. S9A; P = 1.33e-4). As predicted, amplification was associated with higher levels of *MYC* mRNA (Supplementary Fig. S9B). *MYC*-amplified tumors did not exhibit greater genomic instability compared with nonamplified tumors (Supplementary Fig. S9C), indicating that *MYC* amplification is not a proxy for more generalized chromosome-level events. Moreover, metastases expressed higher levels of *MYC* mRNA than primary tumors (Fig. 7C; P = 0.00312). These results indicate that *MYC* amplification and transcriptional upregulation are strongly associated with PDAC metastases.

Next, we examined a separate patient cohort (n = 20) in whom matched primary PDAC tumors and metastases were available for comparison. *MYC* amplifications were common in the primary tumors of patients with metastatic disease (35.0%; n = 7/20), and these amplifications were retained in the matching metastases (Supplementary Fig. S9D), similar to our mouse model. The enrichment of *MYC* amplifications in metastatic samples and the observed retention of the amplification when analyzing matched primary/metastasis samples suggests that amplification and/or transcriptional upregulation of *MYC* in primary PDACs are selected for and retained during tumor metastatic progression. Consistent with this notion, we identified a patient with PDAC in whom single-cell analysis of a paired primary tumor and metastasis revealed enrichment of a *MYC*-amplified subclone in the metastatic lesion compared with the primary (Fig. 7D and E; Supplementary Fig. S9E). Collectively, these data suggest that enhanced expression and/or genomic amplification of *MYC* is associated with metastatic spread in human PDAC, complementing our findings from the mouse model.

DISCUSSION

Phenotypic variation, the result of inter- and intratumoral heterogeneity arising during tumor progression, has made it challenging to understand the molecular mechanisms underlying tumor spread (1, 75). Consequently, the demonstration that certain genes function as "metastasis drivers"—promoting metastasis through mechanisms distinct from their roles in primary tumor growth—has proven elusive (76). In this study, we exploited an autochthonous PDAC model with varying degrees of metastatic spread to explore the molecular basis of naturally arising variation in metastatic burden. This system revealed a strong association between the level of MYC—at either the genomic or transcriptional level—and tumor metastasis, a relationship that was also observed in human PDAC samples. MYC exerts its prometastatic effect at least in part by recruiting proinvasive TAMs, leading to greater tumor cell intravasation into the bloodstream. These activities are not directly related to MYC's well-described role in primary tumor growth (46, 77, 78), as

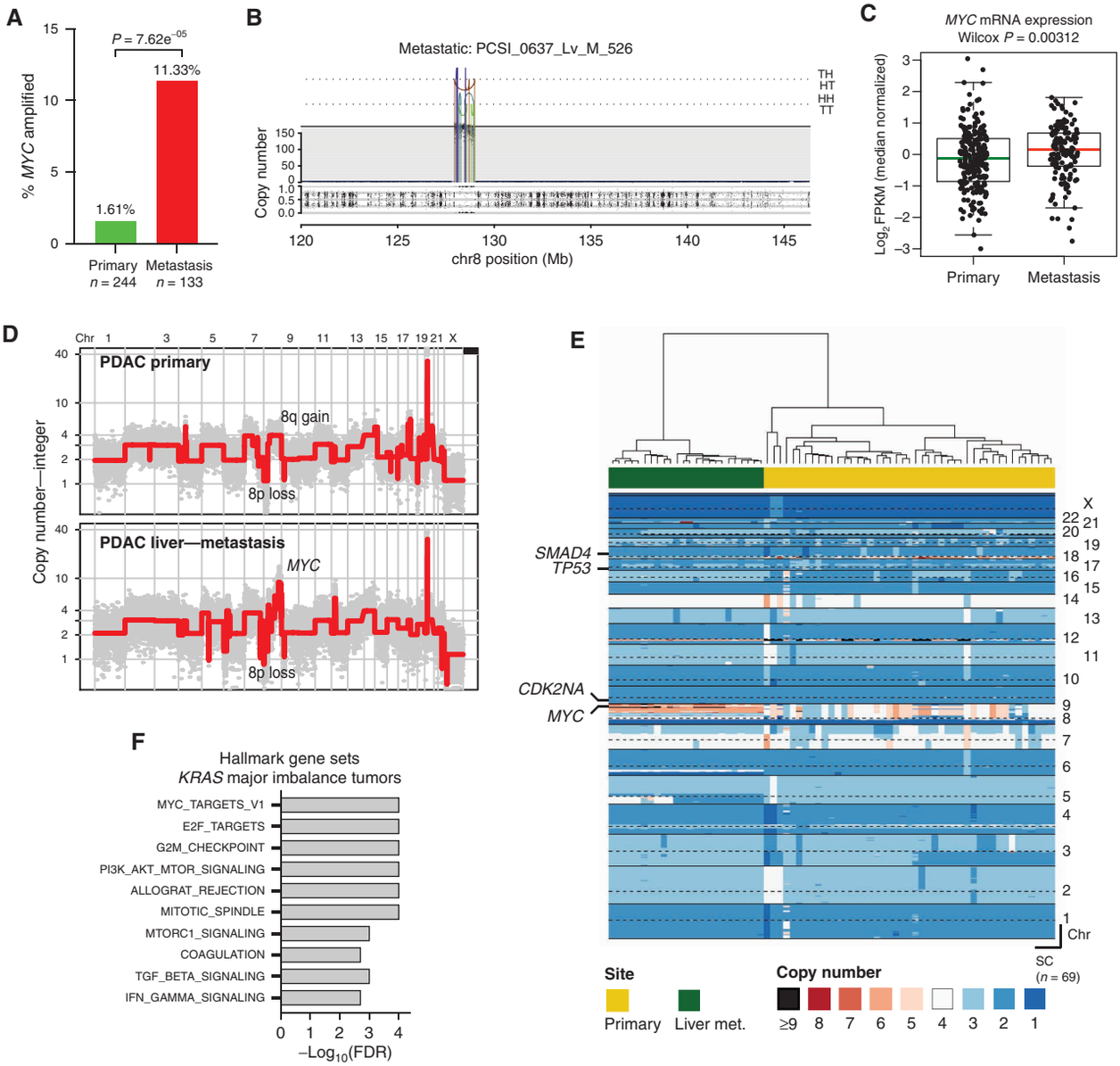

Figure 7. *MYC* amplification and enhanced transcriptional activity are associated with metastasis in human PDAC. **A,** Bar graph showing the relative frequencies of *MYC* amplifications in primary PDAC tumors and metastases from the COMPASS cohort. **B,** Representative plot of chromosome 8 from a metastatic tumor with *MYC* amplification. Orientation of breakpoint junctions from intrachromosomal rearrangements indicated by TH, HT, HH, and TT, where T = tail (3′ end of fragment) and H = head (5′ end of fragment). **C,** Box-and-whisker plot showing *MYC* mRNA levels (fragments per kilobase of exon per million, FPKM) in primary PDAC tumors and metastases. **D,** Representative genome-wide absolute copy-number plots of single cells retrieved from a primary (top) and its matched metastasis (bottom) illustrating acquisition of focal *MYC* amplification in the metastatic lesion. **E,** Heat-map depiction of cancer single cells (SC) sequenced from a matched primary PDAC and its liver metastasis. Color codes indicate absolute copy number in single cells. Top bar plot depicts tissue site from where single cells were retrieved. **F,** GSEA of tumors with a major imbalance of mutant *KRAS* (compared with those with no major imbalance) in the COMPASS cohort. Box-and-whisker plot in **C** indicates mean and interquartile range.

tumors with different levels of *Myc* expression grow at comparable rates despite dramatic differences in metastatic ability.

Prior work by us and others has examined the genetic events associated with PDAC metastasis. In one study, a comparison of matched primary tumors and metastases from four patients failed to reveal nonsynonymous mutations in driver oncogenes that distinguished primary tumors from metastases (79). By contrast, examination of DNA copy-number changes in mouse and human PDAC revealed a significant association between increased mutant *KRAS* gene dosage and metastatic progression (13, 14). Although our mouse studies did not detect an association between *Kras* focal amplification and metastatic potential, *Kras* gains (via entire gain of chromosome 6) were detected with comparable frequency in both Met^{High} and Met^{Low} tumors, consistent with the ability of both tumor populations to metastasize. Interestingly, among

patients with PDAC who had *KRAS* amplifications or major allelic imbalances, the MYC_TARGETS gene set represented the most highly enriched signature (Fig. 7F) in mirroring the enrichment of this signature in *MYC*-amplified PDAC tumors (Supplementary Fig. S9F). Signaling through KRAS has long been known to affect MYC expression (44, 80–82), and thus our results are consistent with a model in which elevated MYC activity—as a result of *MYC* and/or *KRAS* amplification or some other mechanism—enhances metastatic activity. This interpretation is consistent with recent studies of lung, breast, and prostate cancers identifying a link between *MYC* amplification and brain or bone metastasis (37, 38, 83).

Although tumor formation in the KPCXY model results from shared founder mutations ($Kras^{G12D}$ activation and *Trp53* loss), our genomic analysis revealed ongoing somatic events during tumor progression, resulting in heterogeneous patterns of genomic alterations within a given tumor. Such alterations were largely present at the level of copy-number gains and losses rather than point mutations or small insertions/deletions. Although the complexity of genomic rearrangements varied between tumors, the degree of genome instability did not correlate with metastatic burden. Thus, the increase in metastasis observed in Met^{High} tumors is not a function of overall SCNA burden but is instead specific to MYC.

Although subregions within a tumor shared many genomic alterations, consistent with a clonal origin, distinct copy-number alterations were also present, suggesting ongoing subclonal evolution. Clonally related metastases exhibited unique ("private") alterations; however, most copy-number gains and losses were shared with the parental primary tumor clone, suggesting that they were present prior to dissemination. In this respect, it is noteworthy that *MYC* amplifications in human PDAC were far more common in metastases than in primary tumors, including one case in which we were able to trace a metastatic lesion directly to a *MYC*-amplified subclone in the primary tumor. Collectively, these results suggest that subclonal *MYC* amplifications, which have been observed in human primary tumors, provide a selective advantage during metastatic progression (84, 85). Given that our analysis identified a *Myc* signature in tumor Met^{High} clones without *Myc* amplifications, and *MYC* amplifications are present in only 11% of human PDAC metastases, other mechanisms for the increased expression of *MYC* mRNA in PDAC metastases are likely to exist.

As one of the best-studied oncogenes, *MYC* has been associated with multiple tumor-promoting activities (80). Given MYC's role in tumor cell growth and proliferation, one possible explanation for our results is that Met^{High} tumors had an earlier onset and/or grew more rapidly, leading to increased metastasis by mass effect. Against this possibility, we found that tumor size and proliferation rates showed no correlation with metastatic burden in either mouse models or human patients. Likewise, our Met^{High} and Met^{Low} cell lines exhibited dramatic differences in metastatic ability despite giving rise to primary tumors of comparable size. Prior studies have shown that *Myc* overexpression in the pancreas in the context of tumor initiation, without KRAS activation, does not result in PDAC but rather insulinomas (86). By contrast, our work provides evidence that MYC hyperactivation—particularly in the setting of focal, high-amplitude amplification—confers metastatic properties after a primary PDAC is established. These results suggest that genetic context (e.g., mutant Kras status) and timing (e.g., early versus late) may determine whether enhanced tumor growth or promotion of metastasis is the prevalent phenotypic consequence of MYC hyperactivation.

Our studies implicate non–cell-autonomous mechanisms involving the recruitment of TAMs as contributors to metastatic heterogeneity. The ability of TAMs to promote tumor cell invasion is well documented (21, 26, 28, 47, 53, 56–61), a property that is in agreement with our finding that Met^{High} and Myc_OE tumors exhibit enhanced vascular intravasation. Furthermore, MYC expression in tumor cells is known to shape the makeup of the surrounding immune microenvironment, making it more immunosuppressive (39, 45). In line with these observations, we find that Met^{High} tumors are enriched for alternatively activated TAMs and have decreased T-cell infiltration—features that favor metastasis (21, 26, 28, 30, 31, 47, 53, 56–61). Our data thus support a model wherein stochastically arising tumor subclones with elevated levels of MYC alter the TiME to facilitate intravasation and metastasis.

Although the specific molecular mediator(s) of TAM recruitment remain to be fully elucidated, we speculate that MYC acts indirectly by regulating the expression of factors that regulate TAM migration and/or function. Consistent with this, we identified several chemokines/cytokines that were upregulated in Met^{High} tumors and could also be induced by MYC overexpression. Functional validation of these factors identified CXCL3 and MIF as potential mediators of TAM recruitment and associated metastasis. Furthermore, combined inhibition of MIF and CXCR2 significantly reduced both metastasis and TAM invasion. Thus, we hypothesize that multiple secreted factors, as opposed to a single factor, act in concert to drive the MYC-associated increase in proinvasive macrophages.

Most patients with PDAC develop metastases. Our data show that even within this population, the extent of metastatic disease varies widely between patients and affects survival. Although many steps are required for tumor cells to metastasize, our data indicate that bloodstream invasion may be a rate-limiting event for metastasis in PDAC. Our work further suggests that in addition to its well-documented cell-autonomous role in tumor growth, MYC acts non–cell autonomously to promote metastasis. Supporting this, modest overexpression of MYC was previously shown to suffice with KRAS activation to drive PDAC metatsasis in an autochthonous mouse model (44). Given that MYC family members are focally amplified in 28% of human cancers (87), these results have broad implications for metastasis in tumor types other than PDAC (88).

METHODS

Mouse Models

All experiments were performed in accordance with the NIH policies on the use of laboratory animals and approved by the Institutional Animal Care and Use Committee of the University of Pennsylvania. KPCX mice were generated through a series of backcrosses as previously described (32). The $Rosa^{Confetti}$ ("X") reporter allele was

introduced into mutant strains bearing *Pdx1CreER* ("C"), *Kras*^{G12D} ("K"), and *Trp53*$^{fl/+}$ ("P") alleles to obtain *Pdx1CreER*; *Kras*^{G12D}; *Trp53*$^{fl/+}$; *Rosa*^{Confetti} ("KPCX") mice (32). For most experiments, animals were heterozygous for the confetti reporter and also contained a Rosa^{YFP} allele in lieu of the second confetti allele to generate "KPCXY" mice. The YFP reporter was introduced to enable fluorescent lineage labeling of tumors that undergo a "no-color" recombination event in the confetti reporter, as previously described (89). To induce recombination, a suspension of tamoxifen (MP Biomedicals) in corn oil (Sigma-Aldrich) was administered to pups via lactation following oral gavage of the mother with 6 mg of the drug on postnatal days 0, 1, and 2. On average, tumor-bearing KPCXY mice were 14 to 16 weeks of age at time of sacrifice.

Multicolor Image Analysis

Pancreatic tumors and organs from tumor-bearing KPCXY mice were isolated and analyzed by fluorescent stereomicroscopy using a Leica M216FA fluorescent microscope with CFP, YFP, and dsRED filters (Chroma). As previously described (32), distinct colorimetric tumor clones in the primary tumor mass are defined as an anatomically contiguous region of monochromatic cells that share a border with adjacent clones of a different color (Fig. 1E; Supplementary Fig. S1C). To accurately quantify the contribution of different colorimetric tumors to metastases, we used the following criteria to identify KPCXY mice suitable for analysis: (i) presence of at least one metastatic lesion to the liver and/or lung, (ii) two or more tumors present, (iii) each metastatic primary tumor carries a unique fluorescent color, and (iv) metastatic lesions can be linked to a specific tumor based on a shared unique fluorescent lineage label. Using these criteria, we identified a panel of 30 mice with a total of 85 tumors. Metastases were quantified by fluorescent stereomicroscopy. Tumor size was determined using ImageJ (NIH) to measure the largest circumference of each fluorescent tumor.

Murine Tumor and Metastasis Sample Acquisition

Pancreatic tumors and associated liver and lung tissues were isolated from tumor-bearing KPCXY mice. Under fluorescent stereomicroscopy, individual colored tumors were identified and biopsied using a 6-mm punch biopsy. Initial biopsy specimens were placed in 750 μL RNAlater (Sigma-Aldrich) for downstream nucleic acid isolation. Subsequent biopsy specimens were submitted for cell line generation and histology. In tumors in which sufficient tissue was available, additional biopsy specimens were taken from anatomically distinct regions of the tumor to obtain subclonal biopsy specimens for genomic analysis. From seven KPCXY mice, we obtained biopsies from 20 tumors, eight of which were amenable to additional subregional biopsies. Paired primary tumors and metastases from each mouse were identified by shared fluorescent lineage labels. Metastases were harvested by microdissection under fluorescent stereomicroscopy and split, and portions were placed in 500 μL RNAlater for nucleic acid isolation or used directly for cell line generation. The remainder of the tissue was embedded for histology. In total, 56 metastases were isolated for genomic analysis. Although individual liver metastases were of sufficient size for microdissection, lung lesions typically were microscopic and could not be readily isolated for molecular analysis.

Tumor Digestion and Cell Lines

Pancreatic tumors were dissociated into single-cell suspensions through mechanical separation and enzymatic digestion as previously described (90). Murine PDAC cell lines 471_Met^{High}_1, 832_Met^{High}_1, 836_Met^{High}_1, 850_Met^{High}_4, 852_Met^{High}_1, 853_Met^{High}_1, 471_Met^{Low}_2, 832_Met^{Low}_2, 842_Met^{Low}_2, 850_Met^{Low}_1, and 852_Met^{Low}_2 were derived from KPCXY primary tumors that were also evaluated by SCNA and RNA-seq. Murine cell lines were cultured in DMEM/F12 medium supplemented with 5 mg/mL D-glucose (Invitrogen), 0.1 mg/mL soybean trypsin inhibitor type I (Invitrogen), 5 mL/L insulin-transferrin-selenium (ITS Premix; BD Biosciences), 25 μg/mL bovine pituitary extract (Gemini Bio-Products), 5 nmol/L 3,3′,5-triiodo-L-thyronine (Sigma-Aldrich), 1 μmol/L dexamethasone (Sigma-Aldrich), 100 ng/mL cholera toxin (Sigma-Aldrich), 10 mmol/L nicotinamide (Sigma-Aldrich), 5% Nu-serum IV culture supplement (Thermo Fisher Scientific), and antibiotics (gentamicin 150 μg/mL, Gibco; amphotericin B 0.25 μg/mL, Invitrogen) at 37°C, 5% CO_2, 21% O_2, and 100% humidity. Cell lines were maintained and passaged according to ATCC recommended procedures and regularly tested for *Mycoplasma* using the MycoAlert Mycoplasma Detection Kit (Lonza).

Immunofluorescence and Histologic Analysis

Tissue samples were fixed in 4% paraformaldehyde (EMS) at room temperature for 45 minutes, followed by an overnight incubation in 30% weight/volume sucrose solution (Sigma-Aldrich). Samples were then embedded in optimal cutting temperature (Tissue-Tek) and frozen on dry ice. Staining was performed on 10-μm sections by first blocking with 5% donkey serum and 0.1% Tween-20 for 1 hour, followed by overnight incubation with primary antibody diluted in blocking buffer in a humidified chamber. Sections were washed three times in PBS containing 0.1% Tween-20. For immunofluorescence staining, slides were then incubated with DAPI (Life Technologies, 1:1,000) and Alexa fluorophore–conjugated antibodies (Jackson ImmunoResearch). For IHC, slides were first incubated with biotinylated secondary antibodies (Jackson ImmunoResearch) and developed using the ABC HRP and DAB kits per manufacturer protocols (Vectorlabs). Primary antibodies used were as follows: rat anti–Ki-67 (eBioscience, 14–5698–82), rabbit anti–c-Myc (Y69; Abcam, Ab32072), rabbit anti-CD3 (Invitrogen, PA1–29547), rabbit anti-F4/80 (Novus, NBP2–12506), rat antineutrophil (Abcam, NIMP_R14), anti-CD206 (R&D Systems, AF2535), and rabbit anti-Arg1 (Cell Signaling Technology, 93668).

BMDM Isolation

Bone marrow immune cells were isolated as described (91), and 2×10^6 isolated immune cells were plated in a 6-well dish in Iscove's Modified Dulbecco's Medium (IMDM; Gibco, 12440053) supplemented with 10% FBS (Gibco), 1% L-glutamine (Corning, MT25005CI), 1% nonessential amino acids (Corning, 11140076), 1% sodium pyruvate (Gibco, 11360–070), 0.001% 2-mercaptoethanol (Gibco, 21985023), 1% penicillin–streptomycin (Gibco, 15140163), and 20 ng/mL recombinant murine macrophage colony-stimulating factor (M-CSF; PeproTech, 315–02) at 37°C, 5% CO_2, 21% O_2, and 100% humidity. BMDMs were differentiated for 7 days and used by gentle scraping before 10 days.

Macrophage Transwell Migration Assay

Macrophage invasion was assessed using a 12-well transwell chamber with 5- to 8-mm filter inserts (Corning). Tumor cells were plated in the bottom chamber 24 hours before addition of BMDMs. For Figs. 5B and 6F, tumor cells were plated on growth factor–reduced Matrigel (Corning, 356231), which was diluted 1:1 in PBS and plated onto the transwell. In total, 100,000 BMDMs were plated per transwell. After 24 hours, the nonmigrated BMDMs and Matrigel were gently removed with a swab. Cells in the bottom surface (migrated BMDMs) of the membrane were fixed in 4% paraformaldehyde for 15 minutes. DAPI (Fig. 5B; Invitrogen, D21490) or crystal violet stain (Fig. 6F; Sigma-Aldrich, 65092a-95) was added in PBS to the transwells. The membranes were imaged and number of macrophages counted in four random fields. For MIF and CXCR2 inhibition, AZD5069 (MedKoo, 206473; 0.1 mmol/L in DMSO) and ISO-1 (Santa Cruz, sc-204807B; 200 μm in DMSO) were added to tumor

cells in transwells prior to coincubation with the macrophages. The experiment was performed in triplicate and repeated twice.

Macrophage Depletion In Vivo

A total of 10,000 tumor cells were orthotopically injected into the pancreas of NOD.SCID mice. Treatments started 10 days after implantation. GW2580, a CSF1R inhibitor (AdooQ Bioscience, A11959), was dissolved in 0.5% hydroxypropyl methyl cellulose and 0.1% Tween (HPMT) and dosed three times a week at 160 mg/kg by oral gavage. Then, 200 μL clodronate or control liposomes (Liposoma, CP-025–025) was given once per week by intraperitoneal injection. Blood was sampled to confirm depletion. Experimental and control mice were euthanized 14 days after initiation of treatment and analyzed for metastasis and immune cells by flow cytometry. Control and experimental groups were run in at least triplicate.

MIF and CXCR2 Inhibition In Vivo

In total, 50,000 tumor cells were orthotopically injected into the pancreata of NOD.SCID mice. Treatments started 10 days after implantation. The MIF inhibitor ISO-1 (Santa Cruz, sc-204807B) was dissolved in DMSO to make a 0.05-mg/μL stock solution and then diluted to 10 mg/kg in HPMT solution for gavage five times a week. The CXCR2 inhibitor AZD5069 (MedKoo, 206473) was dissolved in HPMT and dosed five times a week at 0.1 mg/kg by oral gavage. Experimental and control mice were euthanized 14 days after treatment start and analyzed for metastasis and immune cells by immunoflouresence staining. Control and experimental groups were run in at least triplicate.

iTEM Assay

The iTEM assay was performed as previously described (50–52). Briefly, transwells from EMD Millipore (MCEP24H48) were coated with 2.5 μg/mL Matrigel (356230, BD Biosciences) in a total volume of 50 μL. Then approximately 1×10^4 human umbilical vein endothelial cells (Lonza) in 50 μL EGM2 medium were plated on the inverted transwells previously coated with Matrigel and allowed to adhere for 4 hours at 37°C. Transwells were then placed into a 24-well plate with 1 mL EGM2 with all supplemental factors (Lonza) in the bottom well and 200 μL inside the top chamber and allowed to grow for 48 hours in order to form a monolayer. Pancreatic tumor cells (EV or Myc_OE) were labeled with CellTracker green dye and macrophages (Bac1.2F5) with CellTracker red (green, C7025, red, C34552; Invitrogen), resuspended in DMEM media (SH30253.01, Hyclone) without serum, and plated at 15,000 pancreatic cancer cells without macrophages or with 60,000 macrophages per transwell and allowed to transmigrate toward EGM2 containing 36 μg/mL of CSF1 for 4 hours. Samples were then fixed in 4% paraformaldehyde for 15 minutes, permeabilized with 1% Triton-X 100 for 5 minutes, and stained with ZO-1 (Sigma-Aldrich) to determine and locate the endothelial monolayer formation. Transwell membranes were cut from the transwell chambers and mounted on a slide using ProLong Diamond antifade (Thermo Fisher Scientific). The slides were imaged using a Leica SP5 confocal microscope using a 60× 1.4 NA objective and processed using ImageJ (NIH). Quantitation was performed by counting the number of tumor cells that had crossed the endothelium within the same field of view (60×, 10 random fields) and represented as normalized values from at least three independent experiments.

Analysis of RNA-seq, Differential Gene Expression, GSEA, and Molecular Subtype

RNA-seq was performed on bulk tumor and metastasis samples from seven KPCX mice, resulting in 66 samples for analysis (primary tumor with subregional biopsy specimens and metastasis). RNA purity and integrity were verified on the Agilent Tapestation prior to library construction, followed by paired-end 50- to 75-bp sequencing on an Illumina HiSeq 4000 high-throughput sequencer. Alignment of fastq files was performed with STAR aligner v2.5.2b using mm10 as the reference genome (92). Gene-level expression data in terms of expected counts and fragments per kilobase of exon per million (FPKM) were obtained using RSEM v1.2.28 (93). Low-expressing genes were removed using a cutoff of 100 for count and 10 for FPKM. For primary tumor clones in which subregional biopsy specimens were taken, count data for the tumor were obtained by merging expression data of the subclone count data using the mean value. This resulted in a total of 54 samples for downstream analysis ($Met^{Low} = 13$, $Met^{High} = 7$, and metastasis = 34). For differential expression analysis, count data were normalized using the voom function in the limma R package followed by batch correction using the ComBat R package (94, 95). Then limma was used to perform differential expression between Met^{High}, Met^{Low}, and metastasis. Box plots of $\log_2$ FPKM values for genes were generated using the ggplot2 R package. To generate volcano plots, differential expression data comparing Met^{Low} and Met^{High} clones were plotted using ggplot2 with log base twofold change from Met^{Low} compared with Met^{High} tumors of each gene plotted on the *x*-axis and the adjusted *P* values plotted on the *y*-axis. Genes with adjusted *P* values < 0.01 and absolute $\log_2$ fold change >1 were highlighted. Differentially expressed genes were used as input for MSigDB GSEA (96). Transcription factor enrichment on all differentially expressed genes was performed using the Metacore software package (Clarivate Analytics). Network analysis was performed on all differentially expressed genes using Ingenuity Pathway Analysis software (Ingenuity Systems, Inc.). Molecular subtype classification using the Moffitt, Bailey, and Collisson (15, 16, 42) signature was performed on each sample by subtracting the sum of normalized expression for genes corresponding to specific classes within a particular molecular signature. We then took the maximum score observed across each class and assigned it to the samples. Heat maps were generated using differentially expressed genes with adjusted *P* value <0.05 and absolute logFC >1.

Survival Analysis of TCGA Data

TCGA pancreatic adenocarcinoma (PAAD) expression and patient- and sample-level clinical data were downloaded from cBioPortal. Samples were filtered to those classified as PAAD and having available expression data (162 of 186 samples). To develop a signature gene list associated with the Met^{High} phenotype, we filtered differentially expressed genes between Met^{High} and Met^{Low} tumors using an adjusted *P* value <0.05 and absolute logFC >0.58, resulting in a set of genes that were upregulated or downregulated in the Met^{High} tumors (736 up and 1,036 down). To calculate a signature score for each TCGA PAAD sample, we first *z* score normalized the TCGA PAAD expression data and then subtracted the sum of all downregulated gene expression from the sum of all upregulated gene expression values. We divided the signature score into high and low strata using a cutoff score >0. Kaplan–Meier analysis was done to compare survival between the two groups.

Human Stage IV Pancreatic Tumor and Metastasis Imaging Analysis

CT scans were obtained from patients with metastatic PDAC undergoing treatment at the University of Pennsylvania under a protocol approved by the Institutional Review Board (#822028). Patients were filtered to include only those with CT scan imaging of the abdomen and chest with intravenous contrast at the time of diagnosis and prior to any treatment and found to have stage IV disease. In total, 55 patients were included. CT images for each patient were reviewed, and metastatic lesions in liver and lung were counted. All metastases were examined in multiple planes to ensure accurate assessment. Tumor area was pulled from the initial radiologist report and measured at the largest diameter. The cutoff for high- and low-metastasis groups was determined using k-means with $n = 2$ clusters.

Human Pancreatic Cancer Patient Sample Acquisition with Genomic and RNA-seq Analysis

Sample acquisition resulted from patients recruited as part of the ICGC Pancreatic Cancer Ductal Adenocarcinoma Canadian sequencing initiative or the COMPASS trial as previously described (97). Tissue samples were collected at the University Health Network (Toronto), Sunnybrook Health Sciences Centre (Toronto), Kingston General Hospital (Kingston), McGill University (Montreal), Mayo Clinic (Rochester), or Massachusetts General Hospital (Boston) with written informed consent and approval from institutional review or research ethics boards. WGS and RNA-seq were performed on fresh-frozen tumor tissue samples that were enriched for tumor content by LCM. WGS and RNA-seq were performed at the Ontario Institute of Cancer Research as described previously (97). DNA read alignment and *MYC* copy-number variations were performed on paired-end whole-exome sequencing reads aligned to human reference genome hg19 using Burrows-Wheeler alignment (BWA) 0.6.2 (98). PCR duplicates were marked with Picard 1.90. Tumor cellularity, ploidy, and copy-number segments were derived using an in-house algorithm, CELLULOID (99). RNA reads were aligned to human reference genome hg38 and to transcriptome Ensemble v84 using STAR v2.5.2a (92). Duplicate reads were marked with Picard 1.121. Raw counts were obtained using HTSeq 0.6.1 (100). Differential gene expression analysis was performed with DESeq2 v.1.14.1 (101) using default settings. Briefly, RNA HTSeq count data were imported to generate a dispersion estimate and a generalized linear model. Wald statistical test was used to compare gene expression of *MYC* amplified to nonamplified cases. GSEA was performed using genes ranked based on the *P* value and sign of the $\log_2$ fold change from differential gene expression analysis. GSEA was run using GSEA Preranked 4.0.2 with default settings against hallmark gene sets (96). Statistical analyses included pairwise comparisons of quantitative variables performed using the Wilcoxon rank sum test. All tests were two-sided. Analyses were carried out in R 3.3.0.

SCNA in Murine Tumors

DNA purified from dissected murine tumors was processed for Illumina library preparation and sequencing using standard protocols. In brief, isolated DNA (100–1000 ng in total) was sonicated on a Covaris instrument. Sonicated DNA was then end-repaired and ligated to TruSeq dual-index library adapters. Index libraries were subsequently enriched by 10 cycles of PCR amplification, followed by pooling and multiplex sequencing targeting a coverage of roughly 2 million reads per sample (102). For data processing and copy-number inference, sequencing data were processed as previously described with mouse genomic bins computed in a manner similar to human bins (36). In brief, sequencing reads were mapped to the mouse reference genome built mm9. Sequencing reads were indexed and sorted, with PCR duplicates removed. Uniquely mapped reads were counted in each bin and normalized for guanine-cytosine content using lowess smoothing. Normalized read count data were then segmented using circular binary segmentation (103) with the profiles centered around a mean of 1. Chromosomal segments with variance that was above or below the mean were called gains or deletions, respectively. A threshold of 0.2 was used. For hierarchical clustering and lineage reconstruction, an analysis based on copy-number values and alteration breakpoints, in a genome-wide manner, was employed.

Bulk and Single-Cell Analysis of Matched Primary and Metastasis from Human Tissue

For 20 patients, tissue sections from flash-frozen samples were processed for bulk DNA purification using the Qiagen DNeasy Blood and Tissue Kit. Purified DNA was processed as described above for multiplex sequencing. A coverage of 2 million sequencing reads was similarly targeted. For a single case, matched pancreatic primary and liver metastasis tissue was retrieved and processed for single-nuclei isolation as previously described (36). Single nuclei were sorted based on DNA content from both diploid and polyploid populations of each tissue. Approximately 100 nuclei per tissue sample were amplified using the WGA4 kit (Sigma-Aldrich), with the resulting whole-genome amplified DNA processed for TruSeq Indexed sequencing library preparation, as described above. Sequencing data were processed as described above with the exception that a least squares fitting algorithm was used to calculate absolute integer copy number (102).

Quantification and Statistical Analysis

Statistical analysis used is indicated in each figure where relevant. All statistical analyses were performed with GraphPad Prism 8 (GraphPad Software). K-means clustering and survival analysis were carried out in R 3.3.0. Error bars show standard deviation or standard error of the mean shown as indicated in the legend, and $P < 0.05$ was considered statistically significant (*, $P < 0.05$, **, $P < 0.005$, and ***, $P < 0.0001$) unless otherwise indicated. *ns* denotes not significant.

Data and Code Availability

The datasets generated during this study are available through the Sequence Read Archive (https://www.ncbi.nlm.nih.gov/sra) under the accession numbers PRJNA647834, PRJNA646123, and PRJNA646156. Additional primary data needed for review or to replicate the findings will be made available on request. Code generated during this study is available at https://github.com/rmaddipati79/Maddipati_PDAC_metastasis.git. Additional detailed methods can be found in the Supplementary Materials and Methods.

Authors' Disclosures

C.A. Adkisson reports a Ruth L. Kirschstein Institutional National Research Service Award during the conduct of the study. J.R. Pitarresi reports grants from the NIH/NCI K99CA252153 and F32CA221094 and the NIH LRP, an American Gastroenterological Association Bern Schwartz Research Scholar Award, a Hopper Belmont Foundation Inspiration Award, and a UPenn P30 Center for Molecular Studies in Digestive and Liver Diseases Pilot and Feasibility Grant outside the submitted work. E.L. Carpenter reports other support from Merck, personal fees from Gordon Conference, Imedex, AHPBA, Bristol Myers Squibb, and GuardantHealth, and grants from UHG outside the submitted work. J.C. McAuliffe reports personal fees from Boston Scientific and nonfinancial support from Loki Therapeutics outside the submitted work. S.W. Lowe reports personal fees and other support from ORIC Pharmaceuticals and Blueprint Medicines, other support from Faeth Therapeutics, and personal fees from PMV Pharmaceuticals outside the submitted work. C.A. Iacobuzio-Donahue reports other support from Bristol Myers Squibb outside the submitted work. B.Z. Stanger reports grants from the NIH during the conduct of the study, as well as personal fees from iTeos Therapeutics and grants from Boehringer Ingelheim outside the submitted work. No disclosures were reported by the other authors.

Authors' Contributions

R. Maddipati: Conceptualization, resources, data curation, formal analysis, supervision, funding acquisition, writing–original draft, project administration, writing–review and editing. **R.J. Norgard:** Conceptualization, data curation, investigation, writing–review and editing. **T. Baslan:** Conceptualization, resources, data curation, investigation, visualization, methodology, writing–original draft, writing–review and editing. **K.S. Rathi:** Data curation, formal analysis, visualization, writing–review and editing. **A. Zhang:** Data curation, formal analysis, visualization, writing–review and editing. **A. Saeid:** Data curation, writing–review and editing. **T. Higashihara:**

Data curation, writing–review and editing. **F. Wu:** Data curation, writing–review and editing. **A. Kumar:** Data curation, writing–review and editing. **V. Annamalai:** Data curation, writing–review and editing. **S. Bhattacharya:** Data curation, writing–review and editing. **P. Raman:** Conceptualization, data curation, supervision, investigation, visualization, writing–review and editing. **C.A. Adkisson:** Data curation, writing–review and editing. **J.R. Pitarresi:** Data curation, formal analysis, writing–review and editing. **M.D. Wengyn:** Data curation, writing–review and editing. **T. Yamazoe:** Data curation, writing–review and editing. **J. Li:** Data curation, writing–review and editing. **D. Balli:** Data curation, formal analysis, writing–review and editing. **M.J. LaRiviere:** Resources, data curation, visualization, writing–review and editing. **T.-V.C. Ngo:** Data curation, writing–review and editing. **I.W. Folkert:** Data curation, writing–review and editing. **I.D. Millstein:** Data curation, writing–review and editing. **J. Bermeo:** Data curation, writing–review and editing. **E.L. Carpenter:** Resources, data curation, writing–review and editing. **J.C. McAuliffe:** Data curation, supervision, writing–review and editing. **M.H. Oktay:** Data curation, supervision, writing–review and editing. **R.A. Brekken:** Data curation, supervision, writing–review and editing. **S.W. Lowe:** Resources, supervision, writing–review and editing. **C.A. Iacobuzio-Donahue:** Resources, supervision, writing–review and editing. **F. Notta:** Resources, formal analysis, supervision, writing–review and editing. **B.Z. Stanger:** Conceptualization, resources, data curation, formal analysis, supervision, funding acquisition, writing–original draft, project administration.

Acknowledgments

We are grateful for helpful advice from Gregory Beatty, Chi Dang, David DeNardo, Rosalie Sears, and all members of the Stanger Laboratory. This work was supported by grants from the NIH (CA229803 to B.Z. Stanger, DK109292 to R. Maddipati, and CA236269 to R.J. Norgard), Cancer Prevention & Research Institute of Texas (RR190029 to R. Maddipati), and American Gastroenterological Association (Caroline Craig and Damian Augustyn Award in Digestive Cancer to R. Maddipati). J.C. McAuliffe is supported by grants from the Albert Einstein Cancer Center (#305631) and a Ruth L. Kirschstein T32 (CA200561). T. Baslan is supported by the William C. and Joyce C. O'Neil Charitable Trust, Memorial Sloan Kettering Single Cell Sequencing Initiative. F. Notta is supported by the Ontario Institute for Cancer Research (OICR), the Canadian Institutes of Health Research (no. 388785), the Cancer Research Society (no. 23383), and the Gattuso-Slaight Personalized Cancer Medicine Fund from Princess Margaret Cancer Centre. Additional support was provided by the Abramson Family Cancer Research Institute, the Abramson Cancer Center, and the NIH/Penn P30 Center for Molecular Studies in Digestive and Liver Diseases (P30DK050306).

The costs of publication of this article were defrayed in part by the payment of page charges. This article must therefore be hereby marked *advertisement* in accordance with 18 U.S.C. Section 1734 solely to indicate this fact.

Note

Supplementary data for this article are available at Cancer Discovery Online (http://cancerdiscovery.aacrjournals.org/).

Received December 20, 2020; revised July 26, 2021; accepted September 17, 2021; published first September 22, 2021.

REFERENCES

1. McGranahan N, Swanton C. Clonal heterogeneity and tumor evolution: past, present, and the future. Cell 2017;168:613–28.
2. Turajlic S, Xu H, Litchfield K, Rowan A, Chambers T, Lopez JI, et al. Tracking cancer evolution reveals constrained routes to metastases: TRACERx renal. Cell 2018;173:581–94.
3. Hunter KW, Amin R, Deasy S, Ha NH, Wakefield L. Genetic insights into the morass of metastatic heterogeneity. Nat Rev Cancer 2018;18:211–23.
4. Gundem G, Van Loo P, Kremeyer B, Alexandrov LB, Tubio JMC, Papaemmanuil E, et al. The evolutionary history of lethal metastatic prostate cancer. Nature 2015;520:353–7.
5. Zhao ZM, Zhao B, Bai Y, Iamarino A, Gaffney SG, Schlessinger J, et al. Early and multiple origins of metastatic lineages within primary tumors. Proc Natl Acad Sci U S A 2016;113:2140–5.
6. Foster CC, Pitroda SP, Weichselbaum RR. Definition, biology, and history of oligometastatic and oligoprogressive disease. Cancer J 2020;26:96–9.
7. Pitroda SP, Weichselbaum RR. Integrated molecular and clinical staging defines the spectrum of metastatic cancer. Nat Rev Clin Oncol 2019;16:581–8.
8. Weichselbaum RR, Hellman S. Oligometastases revisited. Nat Rev Clin Oncol 2011;8:378–82.
9. Deek MP, Tran PT. Oligometastatic and oligoprogression disease and local therapies in prostate cancer. Cancer J 2020;26:137–43.
10. Phillips R, Shi WY, Deek M, Radwan N, Lim SJ, Antonarakis ES, et al. Outcomes of observation vs stereotactic ablative radiation for oligometastatic prostate cancer: the ORIOLE phase 2 randomized clinical trial. JAMA Oncol 2020;6:650–9.
11. Weickhardt AJ, Scheier B, Burke JM, Gan G, Lu X, Bunn PA Jr, et al. Local ablative therapy of oligoprogressive disease prolongs disease control by tyrosine kinase inhibitors in oncogene-addicted non-small-cell lung cancer. J Thorac Oncol 2012;7:1807–14.
12. Ryan DP, Hong TS, Bardeesy N. Pancreatic adenocarcinoma. N Engl J Med 2014;371:1039–49.
13. Mueller S, Engleitner T, Maresch R, Zukowska M, Lange S, Kaltenbacher T, et al. Evolutionary routes and KRAS dosage define pancreatic cancer phenotypes. Nature 2018;554:62–8.
14. Chan-Seng-Yue M, Kim JC, Wilson GW, Ng K, Figueroa EF, O'Kane GM, et al. Transcription phenotypes of pancreatic cancer are driven by genomic events during tumor evolution. Nat Genet 2020;52:231–40.
15. Moffitt RA, Marayati R, Flate EL, Volmar KE, Loeza SG, Hoadley KA, et al. Virtual microdissection identifies distinct tumor- and stroma-specific subtypes of pancreatic ductal adenocarcinoma. Nat Genet 2015;47:1168–78.
16. Bailey P, Chang DK, Nones K, Johns AL, Patch AM, Gingras MC, et al. Genomic analyses identify molecular subtypes of pancreatic cancer. Nature 2016;531:47–52.
17. Campbell PJ, Yachida S, Mudie LJ, Stephens PJ, Pleasance ED, Stebbings LA, et al. The patterns and dynamics of genomic instability in metastatic pancreatic cancer. Nature 2010;467:1109–13.
18. Cancer Genome Atlas Research Network. Integrated genomic characterization of pancreatic ductal adenocarcinoma. Cancer Cell 2017;32:185–203.
19. El-Kenawi A, Hanggi K, Ruffell B. The immune microenvironment and cancer metastasis. Cold Spring Harb Perspect Med 2020;10:a037424.
20. Swierczak A, Pollard JW. Myeloid cells in metastasis. Cold Spring Harb Perspect Med 2019;10:a038026.
21. Kitamura T, Qian BZ, Soong D, Cassetta L, Noy R, Sugano G, et al. CCL2-induced chemokine cascade promotes breast cancer metastasis by enhancing retention of metastasis-associated macrophages. J Exp Med 2015;212:1043–59.
22. Wyckoff J, Wang W, Lin EY, Wang Y, Pixley F, Stanley ER, et al. A paracrine loop between tumor cells and macrophages is required for tumor cell migration in mammary tumors. Cancer Res 2004;64:7022–9.
23. Wellenstein MD, de Visser KE. Cancer-cell-intrinsic mechanisms shaping the tumor immune landscape. Immunity 2018;48:399–416.
24. Wculek SK, Malanchi I. Neutrophils support lung colonization of metastasis-initiating breast cancer cells. Nature 2015;528:413–7.
25. Szczerba BM, Castro-Giner F, Vetter M, Krol I, Gkountela S, Landin J, et al. Neutrophils escort circulating tumour cells to enable cell cycle progression. Nature 2019;566:553–7.

26. Qian BZ, Li J, Zhang H, Kitamura T, Zhang J, Campion LR, et al. CCL2 recruits inflammatory monocytes to facilitate breast-tumour metastasis. Nature 2011;475:222–5.
27. Park J, Wysocki RW, Amoozgar Z, Maiorino L, Fein MR, Jorns J, et al. Cancer cells induce metastasis-supporting neutrophil extracellular DNA traps. Sci Transl Med 2016;8:361ra138.
28. Linde N, Casanova-Acebes M, Sosa MS, Mortha A, Rahman A, Farias E, et al. Macrophages orchestrate breast cancer early dissemination and metastasis. Nat Commun 2018;9:21.
29. DeNardo DG, Barreto JB, Andreu P, Vasquez L, Tawfik D, Kolhatkar N, et al. CD4(+) T cells regulate pulmonary metastasis of mammary carcinomas by enhancing protumor properties of macrophages. Cancer Cell 2009;16:91–102.
30. Li J, Byrne KT, Yan F, Yamazoe T, Chen Z, Baslan T, et al. Tumor cell-intrinsic factors underlie heterogeneity of immune cell infiltration and response to immunotherapy. Immunity 2018;49:178–93.
31. Pommier A, Anaparthy N, Memos N, Kelley ZL, Gouronnec A, Yan R, et al. Unresolved endoplasmic reticulum stress engenders immune-resistant, latent pancreatic cancer metastases. Science 2018;360:eaao4908.
32. Maddipati R, Stanger BZ. Pancreatic cancer metastases harbor evidence of polyclonality. Cancer Discov 2015;5:1086–97.
33. Yachida S, Iacobuzio-Donahue CA. The pathology and genetics of metastatic pancreatic cancer. Arch Pathol Lab Med 2009;133:413–22.
34. Iacobuzio-Donahue CA, Fu B, Yachida S, Luo M, Abe H, Henderson CM, et al. DPC4 gene status of the primary carcinoma correlates with patterns of failure in patients with pancreatic cancer. J Clin Oncol 2009;27:1806–13.
35. Navin N, Krasnitz A, Rodgers L, Cook K, Meth J, Kendall J, et al. Inferring tumor progression from genomic heterogeneity. Genome Res 2010;20:68–80.
36. Baslan T, Kendall J, Rodgers L, Cox H, Riggs M, Stepansky A, et al. Genome-wide copy-number analysis of single cells. Nat Protoc 2012;7:1024–41.
37. Shih DJH, Nayyar N, Bihun I, Dagogo-Jack I, Gill CM, Aquilanti E, et al. Genomic characterization of human brain metastases identifies drivers of metastatic lung adenocarcinoma. Nat Genet 2020;52:371–7.
38. Klotz R, Thomas A, Teng T, Han SM, Iriondo O, Li L, et al. Circulating tumor cells exhibit metastatic tropism and reveal brain metastasis drivers. Cancer Discov 2020;10:86–103.
39. Dhanasekaran R, Baylot V, Kim M, Kuruvilla S, Bellovin DI, Adeniji N, et al. MYC and Twist1 cooperate to drive metastasis by eliciting crosstalk between cancer and innate immunity. Elife 2020;9:e50731.
40. McDonald OG, Li X, Saunders T, Tryggvadottir R, Mentch SJ, Warmoes MO, et al. Epigenomic reprogramming during pancreatic cancer progression links anabolic glucose metabolism to distant metastasis. Nat Genet 2017;49:367–76.
41. Chiou SH, Risca VI, Wang GX, Yang D, Gruner BM, Kathiria AS, et al. BLIMP1 induces transient metastatic heterogeneity in pancreatic cancer. Cancer Discov 2017;7:1184–99.
42. Collisson EA, Sadanandam A, Olson P, Gibb WJ, Truitt M, Gu S, et al. Subtypes of pancreatic ductal adenocarcinoma and their differing responses to therapy. Nat Med 2011;17:500–3.
43. Welch DR, Hurst DR. Defining the hallmarks of metastasis. Cancer Res 2019;79:3011–27.
44. Muthalagu N, Monteverde T, Raffo-Iraolagoitia X, Wiesheu R, Whyte D, Hedley A, et al. Repression of the type I interferon pathway underlies MYC- and KRAS-dependent evasion of NK and B cells in pancreatic ductal adenocarcinoma. Cancer Discov 2020;10:872–87.
45. Kortlever RM, Sodir NM, Wilson CH, Burkhart DL, Pellegrinet L, Brown Swigart L, et al. Myc cooperates with Ras by programming inflammation and immune suppression. Cell 2017;171:1301–15.
46. Sodir NM, Kortlever RM, Barthet VJA, Campos T, Pellegrinet L, Kupczak S, et al. MYC instructs and maintains pancreatic adenocarcinoma phenotype. Cancer Discov 2020;10:588–607.
47. Cassetta L, Pollard JW. Tumor-associated macrophages. Curr Biol 2020;30:R246–R8.
48. Jablonski KA, Amici SA, Webb LM, Ruiz-Rosado Jde D, Popovich PG, Partida-Sanchez S, et al. Novel markers to delineate murine M1 and M2 macrophages. PLoS One 2015;10:e0145342.
49. Harney AS, Arwert EN, Entenberg D, Wang Y, Guo P, Qian BZ, et al. Real-time imaging reveals local, transient vascular permeability, and tumor cell intravasation stimulated by TIE2hi macrophage-derived VEGFA. Cancer Discov 2015;5:932–43.
50. Pignatelli J, Goswami S, Jones JG, Rohan TE, Pieri E, Chen X, et al. Invasive breast carcinoma cells from patients exhibit MenaINV- and macrophage-dependent transendothelial migration. Sci Signal 2014;7:ra112.
51. Cabrera RM, Mao SPH, Surve CR, Condeelis JS, Segall JE. A novel neuregulin–jagged1 paracrine loop in breast cancer transendothelial migration. Breast Cancer Res 2018;20:24.
52. Nicholls DJ, Wiley K, Dainty I, MacIntosh F, Phillips C, Gaw A, et al. Pharmacological characterization of AZD5069, a slowly reversible CXC chemokine receptor 2 antagonist. J Pharmacol Exp Ther 2015;353:340–50.
53. Zhu Y, Knolhoff BL, Meyer MA, Nywening TM, West BL, Luo J, et al. CSF1/CSF1R blockade reprograms tumor-infiltrating macrophages and improves response to T-cell checkpoint immunotherapy in pancreatic cancer models. Cancer Res 2014;74:5057–69.
54. Zhu Y, Herndon JM, Sojka DK, Kim KW, Knolhoff BL, Zuo C, et al. Tissue-resident macrophages in pancreatic ductal adenocarcinoma originate from embryonic hematopoiesis and promote tumor progression. Immunity 2017;47:323–38.
55. Li Z, Xu X, Feng X, Murphy PM. The macrophage-depleting agent clodronate promotes durable hematopoietic chimerism and donor-specific skin allograft tolerance in mice. Sci Rep 2016;6:22143.
56. Cassetta L, Fragkogianni S, Sims AH, Swierczak A, Forrester LM, Zhang H, et al. Human tumor-associated macrophage and monocyte transcriptional landscapes reveal cancer-specific reprogramming, biomarkers, and therapeutic targets. Cancer Cell 2019;35:588–602.
57. Ginter PS, Karagiannis GS, Entenberg D, Lin Y, Condeelis J, Jones JG, et al. Tumor microenvironment of metastasis (TMEM) doorways are restricted to the blood vessel endothelium in both primary breast cancers and their lymph node metastases. Cancers 2019;11:1507.
58. Roh-Johnson M, Bravo-Cordero JJ, Patsialou A, Sharma VP, Guo P, Liu H, et al. Macrophage contact induces RhoA GTPase signaling to trigger tumor cell intravasation. Oncogene 2014;33:4203–12.
59. Steele CW, Karim SA, Leach JDG, Bailey P, Upstill-Goddard R, Rishi L, et al. CXCR2 inhibition profoundly suppresses metastases and augments immunotherapy in pancreatic ductal adenocarcinoma. Cancer Cell 2016;29:832–45.
60. Lee CC, Lin JC, Hwang WL, Kuo YJ, Chen HK, Tai SK, et al. Macrophage-secreted interleukin-35 regulates cancer cell plasticity to facilitate metastatic colonization. Nat Commun 2018;9:3763.
61. Chen Q, Zhang XH, Massague J. Macrophage binding to receptor VCAM-1 transmits survival signals in breast cancer cells that invade the lungs. Cancer Cell 2011;20:538–49.
62. Costa-Silva B, Aiello NM, Ocean AJ, Singh S, Zhang H, Thakur BK, et al. Pancreatic cancer exosomes initiate pre-metastatic niche formation in the liver. Nat Cell Biol 2015;17:816–26.
63. Jia Y, Ji KE, Ji J, Hao C, Ye L, Sanders AJ, et al. IL24 and its receptors regulate growth and migration of pancreatic cancer cells and are potential biomarkers for IL24 molecular therapy. Anticancer Res 2016;36:1153–63.
64. Kodama T, Koma YI, Arai N, Kido A, Urakawa N, Nishio M, et al. CCL3-CCR5 axis contributes to progression of esophageal squamous cell carcinoma by promoting cell migration and invasion via Akt and ERK pathways. Lab Invest 2020;100:1140–57.
65. Miao L, Qi J, Zhao Q, Wu QN, Wei DL, Wei XL, et al. Targeting the STING pathway in tumor-associated macrophages regulates innate immune sensing of gastric cancer cells. Theranostics 2020;10:498–515.
66. Yevshin I, Sharipov R, Valeev T, Kel A, Kolpakov F. GTRD: a database of transcription factor binding sites identified by ChIP-seq experiments. Nucleic Acids Res 2017;45:D61–D7.

67. Yevshin I, Sharipov R, Kolmykov S, Kondrakhin Y, Kolpakov F. GTRD: a database on gene transcription regulation—2019 update. Nucleic Acids Res 2019;47:D100–D5.
68. Dreos R, Ambrosini G, Perier RC, Bucher P. The Eukaryotic Promoter Database: expansion of EPDnew and new promoter analysis tools. Nucleic Acids Res 2015;43(Database issue):D92–6.
69. Dreos R, Ambrosini G, Groux R, Cavin Perier R, Bucher P. The eukaryotic promoter database in its 30th year: focus on non-vertebrate organisms. Nucleic Acids Res 2017;45:D51–D5.
70. Di Mitri D, Mirenda M, Vasilevska J, Calcinotto A, Delaleu N, Revandkar A, et al. Re-education of tumor-associated macrophages by CXCR2 blockade drives senescence and tumor inhibition in advanced prostate cancer. Cell Rep 2019;28:2156–68.
71. Funamizu N, Hu C, Lacy C, Schetter A, Zhang G, He P, et al. Macrophage migration inhibitory factor induces epithelial to mesenchymal transition, enhances tumor aggressiveness and predicts clinical outcome in resected pancreatic ductal adenocarcinoma. Int J Cancer 2013;132:785–94.
72. Wen Y, Cai W, Yang J, Fu X, Putha L, Xia Q, et al. Targeting macrophage migration inhibitory factor in acute pancreatitis and pancreatic cancer. Front Pharmacol 2021;12:638950.
73. Cheng B, Wang Q, Song Y, Liu Y, Liu Y, Yang S, et al. MIF inhibitor, ISO-1, attenuates human pancreatic cancer cell proliferation, migration and invasion in vitro, and suppresses xenograft tumour growth in vivo. Sci Rep 2020;10:6741.
74. Aung KL, Fischer SE, Denroche RE, Jang GH, Dodd A, Creighton S, et al. Genomics-driven precision medicine for advanced pancreatic cancer: early results from the COMPASS trial. Clin Cancer Res 2018;24:1344–54.
75. Turajlic S, Sottoriva A, Graham T, Swanton C. Resolving genetic heterogeneity in cancer. Nat Rev Genet 2019;20:404–16.
76. Lambert AW, Pattabiraman DR, Weinberg RA. Emerging biological principles of metastasis. Cell 2017;168:670–91.
77. Hessmann E, Schneider G, Ellenrieder V, Siveke JT. MYC in pancreatic cancer: novel mechanistic insights and their translation into therapeutic strategies. Oncogene 2016;35:1609–18.
78. Farrell AS, Joly MM, Allen-Petersen BL, Worth PJ, Lanciault C, Sauer D, et al. MYC regulates ductal-neuroendocrine lineage plasticity in pancreatic ductal adenocarcinoma associated with poor outcome and chemoresistance. Nat Commun 2017;8:1728.
79. Makohon-Moore AP, Zhang M, Reiter JG, Bozic I, Allen B, Kundu D, et al. Limited heterogeneity of known driver gene mutations among the metastases of individual patients with pancreatic cancer. Nat Genet 2017;49:358–66.
80. Dang CV. MYC on the path to cancer. Cell 2012;149:22–35.
81. Vaseva AV, Blake DR, Gilbert TSK, Ng S, Hostetter G, Azam SH, et al. KRAS suppression-induced degradation of MYC is antagonized by a MEK5-ERK5 compensatory mechanism. Cancer Cell 2018;34:807–22.
82. Sears R, Nuckolls F, Haura E, Taya Y, Tamai K, Nevins JR. Multiple Ras-dependent phosphorylation pathways regulate Myc protein stability. Genes Dev 2000;14:2501–14.
83. Arriaga JM, Panja S, Alshalalfa M, Zhao J, Zou M, Giacobbe A, et al. A MYC and RAS co-activation signature in localized prostate cancer drives bone metastasis and castration resistance. Nat Cancer 2020;1:1082–96.
84. Hayashi A, Yavas A, McIntyre CA, Ho YJ, Erakky A, Wong W, et al. Genetic and clinical correlates of entosis in pancreatic ductal adenocarcinoma. Mod Pathol 2020;33:1822–31.
85. Baslan T, Kendall J, Volyanskyy K, McNamara K, Cox H, D'Italia S, et al. Novel insights into breast cancer copy-number genetic heterogeneity revealed by single-cell genome sequencing. Elife 2020;9:e51480.
86. Lewis BC, Klimstra DS, Varmus HE. The c-myc and PyMT oncogenes induce different tumor types in a somatic mouse model for pancreatic cancer. Genes Dev 2003;17:3127–38.
87. Schaub FX, Dhankani V, Berger AC, Trivedi M, Richardson AB, Shaw R, et al. Pan-cancer alterations of the MYC oncogene and its proximal network across The Cancer Genome Atlas. Cell Syst 2018;6:282–300.
88. Kruspig B, Monteverde T, Neidler S, Hock A, Kerr E, Nixon C, et al. The ERBB network facilitates KRAS-driven lung tumorigenesis. Sci Transl Med 2018;10:eaao2565.
89. Snippert HJ, van der Flier LG, Sato T, van Es JH, van den Born M, Kroon-Veenboer C, et al. Intestinal crypt homeostasis results from neutral competition between symmetrically dividing Lgr5 stem cells. Cell 2010;143:134–44.
90. Rhim AD, Mirek ET, Aiello NM, Maitra A, Bailey JM, McAllister F, et al. EMT and dissemination precede pancreatic tumor formation. Cell 2012;148:349–61.
91. Liu X, Quan N. Immune cell isolation from mouse femur bone marrow. Bio Protoc 2015;5:e1631.
92. Dobin A, Davis CA, Schlesinger F, Drenkow J, Zaleski C, Jha S, et al. STAR: ultrafast universal RNA-seq aligner. Bioinformatics 2013;29:15–21.
93. Li B, Dewey CN. RSEM: accurate transcript quantification from RNA-Seq data with or without a reference genome. BMC Bioinformatics 2011;12:323.
94. Ritchie ME, Phipson B, Wu D, Hu Y, Law CW, Shi W, et al. limma powers differential expression analyses for RNA-sequencing and microarray studies. Nucleic Acids Res 2015;43:e47.
95. Wang M, Huang J, Liu Y, Ma L, Potash JB, Han S. COMBAT: a combined association test for genes using summary statistics. Genetics 2017;207:883–91.
96. Subramanian A, Tamayo P, Mootha VK, Mukherjee S, Ebert BL, Gillette MA, et al. Gene set enrichment analysis: a knowledge-based approach for interpreting genome-wide expression profiles. Proc Natl Acad Sci U S A 2005;102:15545–50.
97. Connor AA, Denroche RE, Jang GH, Timms L, Kalimuthu SN, Selander I, et al. Association of distinct mutational signatures with correlates of increased immune activity in pancreatic ductal adenocarcinoma. JAMA Oncol 2017;3:774–83.
98. Li H, Durbin R. Fast and accurate short read alignment with Burrows-Wheeler transform. Bioinformatics 2009;25:1754–60.
99. Notta F, Chan-Seng-Yue M, Lemire M, Li Y, Wilson GW, Connor AA, et al. A renewed model of pancreatic cancer evolution based on genomic rearrangement patterns. Nature 2016;538:378–82.
100. Anders S, Pyl PT, Huber W. HTSeq–a Python framework to work with high-throughput sequencing data. Bioinformatics 2015;31:166–9.
101. Love MI, Huber W, Anders S. Moderated estimation of fold change and dispersion for RNA-seq data with DESeq2. Genome Biol 2014;15:550.
102. Baslan T, Kendall J, Ward B, Cox H, Leotta A, Rodgers L, et al. Optimizing sparse sequencing of single cells for highly multiplex copy-number profiling. Genome Res 2015;25:714–24.
103. Venkatraman ES, Olshen AB. A faster circular binary segmentation algorithm for the analysis of array CGH data. Bioinformatics 2007;23:657–63.